TITLE:

The rapid developmental rise of somatic inhibition disengages hippocampal dynamics from self-motion

AUTHORS:

Robin F. Dard[1], Erwan Leprince[1], Julien Denis[1], Shrisha Rao-Balappa[2], Catherine Lopez[1], Marie Giorgi-Kurz[1], Tom Szwagier[1,3], Theo Dumont[1,3], Herve Rouault[2], Marat Minlebaev[1], Agnes Baude[1], Rosa Cossart[1*], Michel A. Picardo[1*]

[1]Aix Marseille Univ, INSERM, INMED (U1249), Turing Centre for Living systems, Marseille, France

[2]Aix-Marseille Univ, Université de Toulon, CNRS, CPT (UMR 7332), Turing Centre for Living systems, Marseille, France

[3] Mines ParisTech, PSL Research University

* Correspondence: michel.picardo@inserm.fr and rosa.cossart@inserm.fr

ABSTRACT:

Early electrophysiological brain oscillations recorded in preterm babies and newborn rodents are initially mostly ignited by bottom-up sensorimotor activity and only later can detach from external inputs. This is a hallmark of most developing brain areas including the hippocampus, which in the adult brain, functions in integrating external inputs onto internal dynamics. Such developmental disengagement from external inputs is likely a fundamental step for the proper development of cognitive internal models. Despite its importance, the exact timing and circuit basis for this disengagement remain unknown. To address this issue, we have investigated the daily evolution of CA1 dynamics and underlying circuits during the first and second postnatal week of mouse development using a combination of two-photon calcium imaging of neuronal somata and axons in non-anesthetized pups, viral tracing and chemogenetics. We show that the first postnatal week ends with an abrupt switch in the representation of self-motion in CA1. Indeed, most CA1 pyramidal cells switch from activated to inhibited by self-generated movements at the end of the first postnatal week whereas GABAergic neurons remain positively modulated throughout this period. This rapid switch occurs within two days and is mediated by the rapid anatomical and functional surge of somatic inhibition. The observed dynamics is consistent with a two-population model undergoing strengthening inhibition. Remarkably, a transient silencing of local somatostatin-expressing interneurons both prevents the emergence of the perisomatic GABAergic coverage and the disengagement of CA1 hippocampal dynamics from self-motion. We propose that such activity-dependent emergence of feedback inhibitory circuits critically inaugurates the development of internal cognitive models.

INTRODUCTION

The adult hippocampus serves multiple cognitive functions including navigation and memory. These functions rely on the ability of hippocampal circuits to integrate external inputs conveying multi-sensory, proprioceptive, contextual and emotional information onto internally-generated dynamics. Therefore, the capacity to produce internally coordinated neuronal activity detached from environmental inputs is central to the cognitive functions of the hippocampus such as planning and memory (Buzsáki, 2015; Buzsáki and Moser, 2013). In contrast to the adult situation, the developing hippocampus, like many developing cortical structures, is mainly driven by bottom-up external environmental and body-derived signals, including motor twitches generated in the spinal cord and/or the brainstem (Dooley et al., 2020; Inácio et al., 2016; Karlsson et al., 2006; Mohns and Blumberg, 2010; Rio-Bermudez et al., 2020; Valeeva et al., 2019). These produce early sharp waves conveyed by inputs from the entorhinal cortex (Valeeva et al., 2019). The emergence of self-organized sequences without reliance on external cues in the form of sharp wave ripples (SWRs) is only observed after the end of the second postnatal week and sequential reactivations even a week later (Farooq and Dragoi, 2019; Muessig et al., 2019). Therefore, early hippocampal activity as measured with electrophysiological recordings is first externally-driven while the emergence of internal dynamics is protracted. The timing and the circuit mechanisms of the switch between motion-guided and internally produced hippocampal dynamics remains unknown. They have been proposed to rely on the maturation of CA3 and extrinsic hippocampal inputs, however, a possible role of local connectivity, in particular recurrent somatic inhibition cannot be excluded.

Local GABAergic interneurons could be critically involved in this phenomenon for several reasons. First, both theoretical and experimental work suggest that self-organized internal neuronal network dynamics require feedback connections to produce an emergent state of activity independently from the incoming input (Hopfield, 1982; Hopfield and Tank, 2005; Yuste, 2015). Feedback circuits are mainly GABAergic in CA1 (but not necessarily inhibitory), given the scarcity of recurrent glutamatergic connections in that hippocampal sub-region (Bezaire and Soltesz, 2013). Second, recent studies indicate that, in the adult CA1 region, parvalbumin-containing (PV) CA1 basket cells contribute to the segregation of self-referenced internal versus externally-driven information into two parallel streams (Lee et al., 2014; Soltesz and Losonczy, 2018; Valero et al., 2015). Basket cells are also long known to mediate the patterning of sharp-wave associated ripples (SWRs), which occur during sleep or quiet immobility, when environmental external influences are minimal (Buzsáki, 2015). However, GABAergic perisomatic cells display a delayed maturation profile both at structural (Jiang et al., 2001; Marty et al., 2002; Morozov and Freund, 2003; Tyzio et al., 1999) and functional levels (Ben-Ari, 2002; Doischer et al., 2008; Khazipov et al., 2004; Murata and Colonnese, 2020). This contributes to the late expression of parvalbumin (from

approximately P15 (Donato et al., 2017)), one main marker of perisomatic GABAergic cells, which adds to the difficulty in studying their early integration into maturing functional circuits (but see (Vormstein-Schneider et al., 2020)).

Here we investigate the evolution of CA1 dynamics during the first and second postnatal weeks of mouse development with an eye on the specific patterning of activity of CA1 GABAergic neurons. To this aim, we adapted two-photon calcium imaging of CA1 dynamics using virally-expressed GCaMP6 through a cranial window in non-anesthetized pups. We show that the first postnatal week ends with an abrupt switch in the representation of self-motion in CA1: principal neurons were synchronized by spontaneous movement before P9, whereas self-motion decreased their activity after that time point. Consistent with a two-population neuronal model, this switch was locally mediated by the rapid anatomical and functional surge of somatic inhibition. Moreover, a transient chemogenetic reduction of activity in somatostatin (SST)-expressing GABAergic neurons prevented both the emergence of somatic GABAergic coverage and the internalization of hippocampal dynamics. This developmental sequence should support the proper emergence of internal cognitive models and as such, may be disrupted in neurodevelopmental disorders, including autism.

MATERIALS AND METHODS

MICE

All experiments were performed under the guidelines of the French National Ethics Committee for Sciences and Health report on "Ethical Principles for Animal Experimentation" in agreement with the European Community Directive 86/609/EEC (Apafis#18-185 and #30-959).

EXPERIMENTAL PROCEDURES AND DATA ACQUISITION

Viruses. *In vivo* calcium imaging experiments were performed using AAV1-hSyn-GCaMP6s.WPRE.SV40 (pAAV.Syn.GCaMP6s.WPRE.SV40 was a gift from Douglas Kim & GENIE Project (Addgene viral prep #100843-AAV1; http://n2t.net/addgene:100843; RRID:Addgene_100843)), AAV9-FLEX-CAG-tdTomato (pAAV-FLEX-tdTomato was a gift from Edward Boyden (Addgene viral prep # 28306-AAV9 ; http://n2t.net/addgene:28306 ; RRID:Addgene_28306)), AAV9-hSyn-FLEX-axon-GCaMP6s (pAAV-hSynapsin1-FLEx-axon-GCaMP6s was a gift from Lin Tian (Addgene viral prep # 112010-AAV9 ; http://n2t.net/addgene:112010 ; RRID:Addgene_112010)). Retrograde tracing experiments were performed using AAV1-hSyn-FLEX-nGToG-WPRE3 (Charité #BA-096) and SAD-B19-RVdG-mCherry (Gift from the Conzelmann laboratory). Inhibitory DREADD expression was

induced in a Cre-dependent manner using AAV9-hSyn-DIO-hM4D(Gi)-mCherry (pAAV-hSyn-DIO-hM4D(Gi)-mCherry was a gift from Bryan Roth (Addgene viral prep # 44362-AAV9 ; http://n2t.net/addgene:44362 ; RRID:Addgene_44362))

Intracerebroventricular injection. This injection protocol was adapted from already published methods (Kim et al., 2014). Mouse pups were anesthetized on ice for 3 – 4 min, and 2 µL of viral solution were injected in the left lateral ventricle whose coordinates were estimated at the 2/5 of the imaginary line between the lambda and the eye at a depth of 0.4 mm. Correct injection was visualized by the spreading of the viral-dye mixture (1/20 of fast blue). In SWISS mouse pups we injected 2 µL of AAV2.1-hSyn-GCAMP6s.WPRE.SV40, in *GAD67Cre* mouse pups we injected either a mix of 1.3µL of AAV2.1-hSyn-GCAMP6s.WPRE.SV40 with 0.7µL of AAV9-FLEX-CAG-tdTomato or 2µL of AAV9-hSyn-FLEX-axon-GCaMP6s.

Intra-hippocampal injection. When hippocampal viral injections were performed at P0 (either AAV1-hSyn-FLEX-nGToG-WPRE3 or AAV9-hSyn-DIO-hM4D(Gi)-mCherry), mouse pups were anaesthetized by inducing hypothermia on ice and maintained on a dry ice-cooled stereotaxic adaptor (Stoelting, 51615) with a digital display console (Kopf, Model 940). Dorsal hippocampus was targeted by empirically determined coordinates, based on the Atlas of the Developing Mouse Brain (Paxinos et al., 2020), using transverse sinus and superior sagittal sinus as reference: 0.8 mm anterior from the sinus intersection; 1.5 mm lateral from the sagittal sinus; 1.1 mm depth from the skull surface. Under aseptic conditions, an incision was made in the skin, the skull was exposed and gently drilled (Ball Mill, Carbide, #¼ .019” -0.500 mm diameter-, CircuitMedic). 10 nL of undiluted viral solution were injected using an oil-based pressure injection system (Nanoject III, Drummond Scientific, rate of 5 nL/min). The tip of the pipette was broken to achieve an opening with an internal diameter of 30-40 µm. When hippocampal viral injections were performed at P5 or P9 (SAD-B19-RVdG-mCherry), pups were anesthetized using 3% isoflurane in a mix of 90% O_2-10% air and maintained during the whole surgery (~0:30 h) between 1% and 2.5% isoflurane. Body temperature was monitored and maintained at 36°C. Analgesia was controlled using Buprenorphine (0.025 mg/ kg). Under aseptic conditions, an incision was made in the skin, the skull was exposed, antero-posterior and medio-lateral coordinates of the dorsal hippocampus were estimated by eye looking at the skull sutures. The skull was gently drilled and 10 nL of a viral solution were injected (Nanoject III, Drummond Scientific, rate of 5 nL/min) at a depth of 1.25 mm below the dura.

Window implant surgery. The surgery to implant a 3-mm-large cranial window above corpus callosum was adapted from previous methods (Villette et al., 2015). Anesthesia was induced using 3% isoflurane in a mix of 90% O_2-10% air and maintained during the whole surgery (~1:30 h) between 1% and 2.5%

isoflurane. Body temperature was controlled and maintained at 36°C. Analgesia was controlled using Buprenorphine (0.025 mg/ kg). Coordinates of the window implant were visually estimated. Then a small custom-made headplate was affixed with cyanoacrylate and dental acrylic cement. The skull was removed and the cortex was gently aspirated until the appearance of the external capsule/alveus. At the end of the cortectomy, we sealed a 3 mm glass window diameter circular cover glass (#1 thickness, Warner Instrument) attached to a 3 mm diameter large and 1.2 mm height cannula (Microgroup INC) with Kwik-Sil adhesive (WPI) and fixed the edge of the glass with cyanoacrylate. We let the animal recover on a heated pad for at least one hour before the imaging experiment.

Imaging. Two-photon calcium imaging experiments were performed on the day of the window implant using a single beam multiphoton pulsed laser scanning system coupled to a microscope (TriM Scope II, LaVision Biotech). The Ti:sapphire excitation laser (Chameleon Ultra II, Coherent) was operated at 920 nm. GCaMP fluorescence was isolated using a bandpass filter (510/25). Images were acquired through a GaAsP PMT (H7422-40, Hamamatsu) using a 16X immersion objective (NIKON, NA 0.8). Using Imspector software (LaVision Biotech), the fluorescence activity from a 400 µm x 400 µm field of view was acquired at approximately 9 Hz with a 1.85 µs dwell time per pixel (2 µm/pixel). Imaging fields were selected to sample the dorsal CA1 area and maximize the number of imaged neurons in the *stratum pyramidale*. Piezo signal, camera exposure time, and image triggers were synchronously acquired and digitized using a 1440A Digidata (Axon instrument, 50 kHz sampling) and the Axoscope 10 software (Axon instrument).

Behavioral recordings. Simultaneously with imaging experiments, mouse motor behavior was monitored. In a first group of animals, motor behavior was monitored using two or three piezos placed below the paws of the animal. The signal from the piezo was acquired and digitized using a 1440A Digidata and the Axoscope 10 software. In a second group of mice, motor behavior was monitored using two infrared cameras (Basler, acA1920-155um) positioned on each side of the animal. For each camera, a square signal corresponding to the exposure time of each frame from the camera was acquired and digitized using a 1440A Digidata and the Axoscope 10 software.

In vivo extracellular electrophysiological recordings. Multisite probes (16 channels silicon probes with 50 um separation distance, NeuroNexus, USA) were used to record electrophysiological activity below the window implant and in the intact hippocampus. To do so, we positioned a P7 pup (that had previously undergone a window implant) on the experimental setup. We slightly anesthetized the animal with a solution of urethane (1 g/kg). To head fix the animal the skull surface was covered with a layer of dental acrylic except the area above the intact hippocampus. In the intact (contralateral) hippocampus the

electrodes were positioned using the stereotaxic coordinates of approximately 1.5 mm anterior to lambda and 1.5 mm lateral from the midline. Hippocampus under the window was recorded through the hole drilled in the window implant. Both multisite silicon probes were positioned at the depth to record *strata oriens* (SO), *pyramidale* (SP), *radiatum* (SR) and *lacunosum moleculare* (SLM). After the positioning of the electrodes, the animal was left in the setup for one hour to recover followed by 2 hours recordings of the neuronal activity in both hippocampi simultaneously.

Drugs. Clozapine N-oxide (CNO) at a dose of 10 mg/kg was administered three times a day via subcutaneous injection. Briefly CNO (Tocris, Ref# 4936, 10mg) was dissolved in 5% DMSO and then diluted with saline solution (DPBS, 14190-144, Life Technologies) to reach a final concentration of 1 mg/mL CNO and 0.25% DMSO. Animals were injected with 10 µL/g of this solution to reach the final dose of 10 mg/kg. Injections were performed during five consecutive days from P3 to P8 every eight hours (0AM-8AM-4PM). During these five days, animal weight was monitored and animals with no increase of body weight within 16 hours were discarded from the experiments. At P9, pups were either used for *in vivo* imaging followed by perfusion and immunohistochemistry or for immunohistochemistry only.

Histological processing. Pups were deeply anaesthetized with a mix of Domitor and Zoletil (0.9 and 60 mg/kg, respectively), then transcardially perfused with 4% PFA in 0.1M PBS (PBS tablets, 18912-014, Life technologies). For perisomatic innervation analysis, brains were post-fixed overnight at 4°C in 4% PFA in 0.1M PBS, washed in PBS, cryo-protected in 30% sucrose in PBS, before liquid nitrogen freezing. Brains were then sectioned using a cryostat (CM 3050S, Leica) into 50 µm thick slices collected on slides. Sections were stored at -20°c until further usage. For tracing experiments, brains from GAD67Cre and *Emx1Cre* pups, were post-fixed overnight at 4 °C in 4% PFA in 0.1M PBS, washed in PBS and sectioned using a vibratome (VT 1200 s, Leica) into sagittal 70–80 µm thick slices. Sections were stored in 0.1M PBS containing 0.05% sodium azide until further usage. Immunocytochemistry was processed as described previously (Bocchio et al., 2020) . Briefly, sections were blocked with PBS-Triton (PBST) 0.3% and 10% normal donkey serum (NDS), and incubated with a mix of up to three primary antibodies simultaneously diluted in PBST with 1% NDS overnight at room temperature with the following primary antibodies: rabbit anti-dsRed (1:1000; Clontech, AB_10013483), chicken anti-GFP (1:1000, Aves Labs, GFP-1020, AB_10000240), mouse anti-synaptotagmin-2 (1:100; Developmental Studies Hybridoma Bank, AB_2315626), goat anti-somatostatin (1:100, Santa Cruz, s c-7819, AB_2302603). After several washes, according to the mixture of primary antibodies, the following secondary antibodies were used: donkey anti-chicken Alexa 488 (1:500, SA1-72000), donkey anti-rabbit Alexa 555 (1:500, ThermoFisher, A31570), donkey anti-sheep Alexa 405 (1:500, Jackson IR, 713-475-

147), donkey anti-mouse Alexa 488 (1:500, ThermoFisher, A21202), donkey anti-mouse Alexa 647 (1:500, ThermoFisher, A31571). After Hoechst counterstaining, slices were mounted in Fluoromount. Epifluorescence images were obtained with a Zeiss AxioImager Z2 microscope coupled to a camera (Zeiss AxioCam MR3) with an HBO lamp associated with 470/40, 525/50, 545/25, and 605/70 filter cubes. Confocal images were acquired with a Zeiss LSM-800 system equipped with a tunable laser providing excitation range from 405 to 670 nm. For quantifying synaptotagmin-2, 11µm thick stacks were taken (z=1µm, pixel size=0,156µm) with the confocal microscope using a plan-Achromat 40x/1,4 Oil DIC objectif.

DATA PREPROCESSING

Motion correction. Image series were motion corrected either by finding the center of mass of the correlations across frames relative to a set of reference frames (Miri et al., 2011) or using the NoRMCorre algorithm available in the CaImAn toolbox (Pnevmatikakis and Giovannucci, 2017) or both.

Cell segmentation. Cell segmentation was achieved using Suite2p (Pachitariu et al., 2017) . Neurons with pixel masks including processes (often the case for interneurons located in the stratum oriens) were replaced by soma ROI manually drawn in ImageJ and matched onto Suite2p contours map using CICADA (**C**alcium **I**maging **C**omplete **A**utomated **D**ata **A**nalysis, source code available on Cossart lab GitLab group ID: 5948056). In experiments performed on *GAD67Cre* animals, tdTomato labelled interneurons were manually selected in ImageJ and either matched onto Suite2p contours map or added to the mask list using CICADA.

Axon segmentation. Axon segmentation was performed using pyAMNESIA (a **Py**thon pipeline for analysing the **A**ctivity and **M**orphology of **NE**urons using **S**keletonization and other **I**mage **A**nalysis techniques, source code available on Cossart lab GitLab group ID: 5948056). pyAMNESIA proposes a novel image processing method based on 3 consecutive steps: 1) extracting the axonal morphology of the image (skeletonization), 2) discarding the detected morphological entities that are not functional ones (branch validation), and 3) grouping together branches with highly correlated activity (branch clustering). To extract the skeleton, we first perform 3D gaussian smoothing and averaging of the recording, producing an image that summarizes it; on this image are then successively applied a histogram equalization, a gaussian smoothing, an adaptive thresholding, and finally a Lee skeletonization (Suen et al., 1994), allowing for the extraction of the skeleton mask and the morphological branches. To ensure the functional unity of the segmented branches, we only kept those that illuminated uniformly, where uniformity was quantified by the skewness of the pixel distribution of the branch during a calcium

transient (branch validation). To cluster the valid branches based on their activity, we first extracted their average trace -- being the average image intensity along the branch for each frame -- and then cluster the branches traces using t-SNE and HDBSCAN algorithms with Spearman correlation metric (branch clustering).

Cell type prediction. Cell type prediction was done using the DeepCINAC cell type classifier (Denis et al., 2020). Briefly, a neuronal network composed of a convolutional neuronal network (CNN) and Long Short Term Memory (LSTM) was trained using labelled interneurons, pyramidal cells and noisy cells to predict the cell type using 100 frames long movie patches centered on the cell of interest. Each cell was classified as interneuron, pyramidal cell or noise. Cells classified as 'noisy cells' were removed from further analysis. 'Labelled interneurons' were first kept in a separate cell type category and added to the interneurons list.

Activity inference. Activity inference was done using DeepCINAC classifiers (Denis et al., 2020). Briefly, a classifier composed of CNN and LSTM was trained using manually-labelled movie patches to predict neuronal activation based on movie visual inspection. Depending on the inferred cell type, activity inference was done using either a general classifier or an interneuron-specific classifier. Activity inference resulted in a (cells x frames) matrix giving the probability for a cell to be active at any single frame. We used a 0.5 threshold in this probability matrix to obtain a binary activity matrix considering a neuron as active from the onset to the peak of a calcium transient.

Behavior. Piezo signals were manually analyzed in a custom-made graphical user interface (Python Tkinter) to label the onset and offset of 'twitches', 'complex movements' and 'unclassified movements'. Twitches were defined as brief movements (a few hundred milliseconds-long) occurring within periods of rest and detected as rapid deflections of the piezo signal. 'Complex movements' were defined as periods of movement lasting at least 2 seconds; 'unclassified movements' were short movements that differed from twitches. Analysis of video tracking was done using CICADA and behavior was manually annotated in the BADASS (Behavioral Analysis Data And Some Surprises) GUI.

Neurodata without border (NWB) embedding. All pre-processed datasets per imaging session were combined into a single NWB file containing imaging data and metadata, cell contours, cell type prediction, neuronal activity inference and animal behavior.

MODELING

Network implementation. We constructed a simple rate model and subsequently a more realistic spiking network in order to test our hypothesis that an increase in perisomatic inhibition could explain the switch in network dynamics between the first and second postnatal week. Both models consisted of one excitatory and one inhibitory population with recurrent interactions (**Figure 5A**, supplementary methods). The development of perisomatic innervation was simulated by increasing the strength from inhibitory to excitatory cells (JEI). The external input to the model was composed of a constant and a white noise term. To estimate the responses to twitch-like inputs, an additional feedforward input composed of short pulses was fed to the network. In the rate model, the rates represented the population averaged activities. The spiking network was constructed with Leaky Integrate and Fire (LIF) neurons. The network connectivity was sparse and each neuron received inputs from randomly selected neurons. Presynaptic spikes resulted in exponentially decaying postsynaptic currents.

DATA ANALYSIS

Histological quantifications. Confocal images of synaptotagmin-2 immunostaining were analyzed using RINGO (RINGs Observation), a custom made macro in Fiji. We first performed a max-intensity projection of the Z-stack images of the top 6 µm from the slice surface, then images were cropped to restrict the analysis to the pyramidal cells layer. Obtained images were denoised using Fiji "remove background" option and then by subtracting the mean intensity of the pixels within a manually drawn ROI in the background area (typically the cell body of a pyramidal neuron). Denoised images were then binarized using a max-entropy thresholding (Fiji option). Finally particles with size between 0.4 μm^2 and 4 μm^2 were automatically detected using the Fiji "Analyse particle" option. We then computed the proportion of the pyramidal cell layer (i.e. surface of the cropped region) covered by positive synaptotagmin-2 labelling.

In vivo electrophysiology. The neuronal activity recorded from both hippocampi *in vivo* using a 64-channel amplifier (DIPSI, France) was analyzed post-hoc. Firstly, data was down sampled to 1 kHz to save disc space. The local field potential (LFP) was high passed (>1 Hz) and the common reference was subtracted to exclude the possible bias produced by volume conducted deflections of LFP. Early sharp-wave events (eSWs) were next detected using a threshold approach. Events were considered as eSWs if: i) LFP reversion was observed in the *stratum pyramidale (SP)* and ii) their peak amplitude in *stratum radiatum (SR)* exceeded the threshold of 4 standard deviations calculated over the entire trace (this conservative threshold corresponds to p values below 0.01). The occurrence rate of eSW was calculated

over 10 minutes-long periods. eSW co-occurrence was also calculated by cross-correlating the eSW timestamps from ipsilateral and contralateral hippocampi using a bin size of 10 milliseconds.

Analysis of calcium imaging data. Analysis was performed using CICADA (v 1.0.6 - all codes are available on the Cossart lab Gitlab, group ID 5948056), a custom-made toolbox allowing for the automatic analysis of calcium imaging data in the NWB format.

Calcium transient frequency analysis. The transient frequency for each cell was computed using the number of calcium event onsets and was averaged across all cells imaged in one given pup across one or more imaging sessions.

Synchronous Calcium Event (SCE) detection. Synchronous Calcium Events were defined as the imaging frames within which the number of co-active cells exceeded chance level as estimated using a reshuffling method. Briefly, an independent circular shift was applied to each cell to obtain 300 surrogate raster plots. We computed the 99th percentile of the distribution of the number of co-active cells from these surrogates and used this value as a threshold to define the minimal number of significantly co-active cells. To estimate the percentage of transients within SCEs we counted, for all cells, the number of calcium transients occurring within SCEs and divided it by the total number of transients of the cell. We averaged the obtained values over all the cells imaged per animal.

Peri-Movement-Time-Histograms (PMTH). A 20 seconds-long time-window centered on movement onset was used. For each movement within an imaging session, the number of cells activated or the sum of all cells fluorescence were calculated for each time bin in that window. In this way, we obtain as many values as movements per time bin; the 25th and 75th percentiles of the distributions of these values per time bin are computed and divided by the number of cells. To combine imaging sessions within age groups (*i.e.* P5-6, 7-8, 9-10, 11-12) all the median, 25th and 75th percentiles were aligned per age group and the median value of the median values, the 25th percentile of the 25th percentile values and the 75th percentile of the 75th percentile values were computed. To display the percentage of active cells at a given time bin, these values were multiplied by 100. Raw outcome values were used to calculate fluorescence. To evaluate chance level around movement onsets, 500 surrogate raster plots per imaging session were computed, and the above procedure was used.

Movement-related activation or inhibition. A 4 seconds-long window centered on the onset of movements was used. The total number of cells activated during this time period was calculated. If at least 60% of these cells were activated within 2s following movement onset, then the movement was classified as 'activator'. If less than 40% of these cells were activated within 2s following movement

onset, the movement was classified as 'inhibitor'. Other cases between 40% and 60 % were classified as 'neutral' movements.

Movement- and immobility-associated cells. The number of transients per cell occurring during movement or rest was calculated. These transients were then reshuffled 100 times using independent circular shifts and the same calculation was performed on each roll. We used the 99th percentile of this distribution as a threshold above which the cell was considered as associated with rest or immobility. Finally, the proportion of cells associated with rest or immobility was calculated for each imaged mouse.

Statistics. Statistical tests were performed using GraphPad (Prism). We used either Kruskall-Wallis or one-way ANOVA to assess the main effect of a given parameter followed by *post hoc* Dunn's multiple comparison or Bonferroni tests if a main effect was detected. We used One-sample t-tests to compare observed and theoretical means in the case of a normal distribution of values (Kolmogorov-Smirnov test).

RESULTS

Highly correlated spontaneous activity dominates CA1 dynamics until the end of the first postnatal week

In order to induce stable and early expression of the calcium indicator protein GCaMP6s, pups were injected with the AAV1-hSyn-GCaMP6s.WPRE.SV40 virus intracerebro-ventricularly on the day of birth (P0, **Figure 1A, S1A**). Five to twelve days after injection, the hippocampal CA1 region of non-anesthetized pups was imaged through a window implant placed on the same day (**Figure 1A, see methods**). This acute window implant did not alter hippocampal dynamics as revealed by *in vivo* bilateral silicon probes electrophysiological recordings of early sharp waves (eSW) in operated pups expressing GCaMP6s (with a frequency of 10 eSW/min (25% 6 eSW/min, 75% 13 eSW/min) for ipsilateral and 10 eSW/min (25% 8 eSW/min, 75% 12 eSW/min) for the contralateral side (**Figure S1B**). eSW synchronisation between hemispheres was also preserved, in agreement with previous data (Graf et al., 2021; Valeeva et al., 2019). We examined 4 age groups, postnatal days 5 to 6 (P5-6, n=6 mice, 11 movies, **see Movie 1**), P7-8 (n=9 mice, 17 movies, **see Movie 2**), P9-10 (n=7 mice, 14 movies, **see Movie 3**) and P11-12 (n=5 mice, 7 movies, **see Movie 4**). The contours of imaged neurons and calcium events were determined using Suite2P and DeepCINAC respectively (Denis et al., 2020; Pachitariu et al., 2017). Consistent with previous electrophysiological studies (Mohns and Blumberg, 2008; Valeeva et al., 2019), spontaneous neuronal activity in the CA1 region of P5-6 pups alternated between recurring population bursts (Synchronous Calcium Events, SCE), and periods of low activity (**Figure 1B first panel**). Hence, until P8, more than half of the detected calcium transients occurred within SCEs (P5-6: 57 +/- 5 %, P7-8:

50 +/- 4 %, n=6 mice and n=9 mice respectively, **Figure 1C)**. Starting from P9-10 (**Figure 1B third panel**), neuronal activity also significantly occurred outside of the SCEs (P9-10: 43 +/-5 %, n=7, P5-6 vs P9-10 $p<0.05$, **Figure 1C**). Finally, at P11-12, most of the activity was observed outside of the SCEs (P11-12: 37 +/- 5%, n=5 mice, P5-6 vs P11-12, $p<0.001$, **Figure 1B last panel, Figure 1C**). Overall, SCE participation rate was significantly affected by age from P5 to P12 (**Figure 1C**, p=0.0002). These changes in CA1 dynamics are not supported by a change in the activation rate of individual neurons as this parameter remained stable across the developmental period studied here (**Figure 1D**). We conclude that the end of the first postnatal week marks the desynchronization of CA1 early dynamics in developing mouse pups.

Early synchronous calcium events correlate with spontaneous motor activity

CA1 dynamics have been reported to follow spontaneous motor activity during the first postnatal week in developing rodents using extracellular electrophysiological recordings (Karlsson et al., 2006; Rio-Bermudez et al., 2020; Valeeva et al., 2019). Hence, we next examined the relationship between population activity and movement as monitored using either piezo recordings or infrared cameras (see methods). We first computed peri-movement time histograms (PMTH) plotting the fraction of active neurons centered on the onset of all movements. During the first postnatal week, movements were followed by an increase in the percentage of active cells (**Figure 2A**, P5-6: n=6 mice, peak value 4.3 % of active cells, P7-8: n=9 mice, peak value 2.4 % of active cells). In contrast, starting from P9-10, movements were not followed by an increase of activity anymore (**Figure 2A,** P9-10: n=5 mice and P11-12: n=4 mice). Short myoclonic movements such as twitches/startles (happening during periods of active sleep (Gramsbergen et al., 1970; Jouvet-Mounier and Astic, 1968; Karlsson et al., 2006), and longer movements (essentially happening during wakefulness) may lead to different activity patterns in the hippocampus (Mohns and Blumberg, 2008). However, when considering separately twitches and longer movements, we found that both resulted in a similar effect on CA1 averaged activity (**Figure S2A**). We thus combined all types of movements in further analysis. We next computed the fraction of movements that were followed by an increase or a decrease in activity (activator or inhibitor movements, respectively, see methods), or no change (neutral movements, see methods, **Figure S2B**). For simplification purposes, we focused on the developmental course of inhibitor movements (age effect, p=0.0071). The proportion of inhibitor movements was similar at P5-6 and P7-8 (P5-6: 14% +/- 11, n=6 mice, P7-8: 15% +/- 8, n=9 mice, **Figure 2B**). Consistent with previous results, the end of the first postnatal week marked a switch with an increase of inhibitor movements at P9-10 (P9-10: 33% +/- 17, n=5 mice) and P11-12 (P11-12: 50% +/-6, n=4 mice, P5-6 vs P11-12 and P7-8 vs P11-12, $p<0.05$, **Figure 2B**). Last, we quantified the proportion of neurons whose activity was preferentially modulated by movement or immobility (**Figure**

2C, see Methods). The proportion of neurons significantly associated with movements gradually decreased with age (age effect, p=0.0201), with a significantly lower fraction at P11-12 compared to P5-6 (P5-6 median 52%, n=6, P11-12 median 12%, n= 4, p<0.05, **Figure 2C left panel**). Conversely, the fraction of neurons significantly associated with immobility increased with age (age effect, p=0.0073), with a significantly higher ratio at P11-12 than P5-6 (P5-6 median 9%, n=6, P11-12 median 47%, n= 4, p<0.01). Altogether, these results indicate that the end of the first postnatal week marks a transition in the evolution of CA1 dynamics, with both a decorrelation and an internalization of neuronal activity. We next investigated the circuit mechanisms supporting these changes.

GABAergic neurons remain activated by spontaneous movement throughout the two first postnatal weeks

As a first step to identify the circuit mechanisms for this switch, we focused on local circuits and disentangled the respective contribution of local GABAergic neurons and principal cells to CA1 dynamics as well as their relation to movement. To this aim, we identified GABAergic neurons by the expression of a red reporter tdTomato in *GAD67Cre* pups virally infected with AAV9-FLEX-tdTomato and AAV1.hSyn.GCaMP6s (**Figure 3A**). In addition, we used these imaging experiments to train a cell classifier that could infer interneurons in the absence of any reporter with a precision of 91.2% (Denis et al., 2020) “labelled” and “inferred” GABAergic neurons were combined into a single group referred to as “interneurons" in the following (**Figure S4**). As illustrated in a representative raster plot from a P5 mouse, both pyramidal cells (green) and interneurons (red) seemed activated during movement (vertical grey lines**, Figure 3A**). This was confirmed when computing the PMTH for pups aged less than P9 (P5-6: n=6 mice, pyramidal cells: peak value 3.4%, interneurons: peak value 9.4%, P7-8: n=9 mice, pyramidal cells: peak value 1.9%, interneurons: peak value 7.3%, **Figure 3B**). In line with previous results (**Figure 2A**), pups older than P9 showed a reduction in the proportion of active pyramidal cells following movement (**Figure 3A, 3B**, P9-10: n=5 mice, P11-12: n=4 mice) as well as a decrease with age in the fraction of movement-associated pyramidal cells (**Figure 3C left panel**, age effect for pyramidal cells p=0.0136). In P5-6 animals, 47% of pyramidal cells (median value) were associated with movement as compared with only 10% (median value) in P11-12 animals (**Figure 3C left panel,** P5-6 n=6 mice vs P11-12: n=4 mice, p<0.05). Conversely, the proportion of pyramidal cells associated with periods of immobility increased (**Figure 3C right panel,** age effect for pyramidal cells p=0.0086) and was significantly different when comparing P11-12 with P5-6 pups (P5-5: n=6 mice, median value=7%; P11-12: n=4 mice, median value=51%, p<0.05). In contrast, interneurons remained activated following movement even past P9 (**Figure 3A and B,** P9-10: n=5 mice, interneurons: peak value 4.8%, P11-12: n=4 mice, interneurons: peak value 9.5%). Accordingly, the proportion of interneurons associated with movement or immobility

did not significantly change between P5-6 and P11-12 (**Figure 3C**). We conclude that the link between movement and activity evolves differentially towards the start of the second postnatal week when comparing pyramidal neurons and GABAergic interneurons, the former being inhibited or detached from movement while the latter remained activated. This suggested that pyramidal neurons could be directly inhibited by interneurons after the first postnatal week, following a functional maturation of GABAergic outputs onto principal cells. Alternatively, this could result from differential changes in the synaptic inputs driving both cell types. We have addressed in the following both, non-mutually exclusive, hypotheses.

We first compared the time course of development of extra-hippocampal synaptic afferences onto CA1 GABAergic neurons and pyramidal cells using a rabies retrograde tracing method (Wickersham et al., 2007) . We focused on changes that may occur around the end of the first postnatal week. To do so, two groups were compared, an *early* (AAV1-hSyn-FLEX-nGToG-WPRE3 -Helper virus- injected at P0, SAD-B19-RVdG-mCherry -pseudotyped defective rabies virus- at P5 and IHC at P9, **Figure S3A**) and a *late* one (AAV1-hSyn-FLEX-nGToG-WPRE3 -Helper virus- injected at P0, SAD-B19-RVdG-mCherry -pseudotyped defective rabies virus- at P9, IHC at P13, **Figure S3D**). Injections were performed in either *GAD67Cre* or *Emx1Cre* pups in order to specifically target GABAergic or glutamatergic cells. Four *GAD67Cre* pups (2 early and 2 late injections) and three *Emx1Cre* pups (1 early and 2 late) were analyzed as injection sites were restricted to the hippocampus. Starter and retrogradely labelled cells were found all over the ipsilateral hippocampus (**Figure S3B, C, E, F**). For both *GAD67Cre* and *Emx1Cre* pups, we found no striking difference in the retrogradely labelled extra-hippocampal regions between *early* and *late* groups (**Figure S3B, C, E, F**). In agreement with previous studies (Supèr and Soriano, 1994), we found that GABAergic and glutamatergic neurons in the dorsal hippocampus received mainly external inputs from the entorhinal cortex, the medial septum and the contralateral CA3 area (retrogradely labelled cells in these regions were found in 4 out of 4 *GAD67Cre* pups and 3 out of 3 *Emx1Cre* pups, **Figure S3**). Therefore, we next explored the maturation of local somatic GABAergic innervation given previous reports of its rapid evolution across this period (Jiang et al., 2001; Marty et al., 2002; Morozov and Freund, 2003) as well as the appearance of a dense tdTomato signal in the pyramidal layer from *GAD67Cre* mouse pups at P12, not visible at P5 (**Figure 3A**).

Abrupt emergence of a functional somatic GABAergic innervation at the beginning of the second postnatal week

We first analyzed the anatomical development of somatic GABAergic innervation within the CA1 pyramidal layer from P3 to P11, focusing on the innervation from putative parvalbumin-expressing

Basket Cells (PVBCs), its main contributor. To this aim, we performed immunohistochemistry against Synaptotagmin2 (Syt2) which has been described as a reliable marker for parvalbumin positive inhibitory boutons in cortical areas (**Figure 4A**, (Sommeijer and Levelt, 2012)). Using a custom made Fiji-plugin (RINGO, see methods), we quantified the surface of the pyramidal cell layer covered by Syt2 labelling at different stages and found that between P3 and P7 PV innervation remains stable (median values: P3: 0.34%, P5: 0.57%, P7: 0.49%, 3 mice per group, **Figure 4B**). However, around P9, a sudden increase in the density of positive labelling was observed (P9: 1.03%, P11: 1.48%, 3 mice per group, **Figure 4B**). These results are consistent with previous work (Jiang et al., 2001; Marty et al., 2002), as well as with our tdTomato labelling (**Figure 3A**). It also perfectly matches the transition observed in CA1 dynamics (**Figure 3**). We next tested whether GABAergic axons in the pyramidal layer were active during periods of movement. In order to increase success rate for imaging axons in the pyramidal layer, we restricted these experiments to P9-10, i.e. when axons start densely innervating the CA1 layer. To do so, we restrained the expression of the calcium indicator GCaMP6s to the axon (Broussard et al., 2018) of interneurons using *GAD67Cre* mouse pups and specifically image axonal arborisation in the pyramidal cell layer (**Figure 4C, left panel**). Fluorescence signals were extracted from axonal branches as defined using PyAmnesia (see methods, **Figure 4C, right panel)**, and then normalized using z-score (see methods). As expected (**Figure 3B)**, an increase in the fluorescent signal of GABAergic axonal branches was observed following movement (P9-10: n=3 mice, max z-score value 0.42, **Figure 4D**). As a result, we reasoned that an increase in perisomatic GABAergic inhibition could potentially contribute to the reduction of activity observed after movement during the second postnatal week in pyramidal neurons.

Increasing feedback inhibition in two-population models reproduces the developmental transition

To test whether an increase in perisomatic inhibition alone can explain the switch in network dynamics between the first and second postnatal week, we simulated a two-population network mimicking the development of perisomatic innervation (**Figure 5A**, see methods). Using a rate model and a Leaky Integrate and Fire model, we show that increasing the strength of perisomatic inhibition can account for the experimentally observed decrease of responses to movement-like feedforward inputs (**Figure 5B**). When inhibition is weak, the average activity of the pyramidal neurons increases at the onset of a given twitch. Then, it quickly relaxes to the baseline with a timescale that follows the synaptic time constant (**Figure 5B**, left panel). In the presence of strong inhibition, there is a reduction in response to movement inputs. In addition, due to strong feedback inhibition following the movement responses, network activity relaxes to the baseline with an undershoot (**Figure 5B**, right panel), recapitulating the experimental findings (**Figure 2A**).

To further show the importance of recurrent network interactions, we computed an autocorrelogram of the experimental network activity from two different groups (P5-9 blue curve, P10-12 orange curve, **Figure 5C, left panel**). Our analytical models displayed similar activity correlograms as the experimental data, with an undershoot in the presence of strong inhibitory feedback. We showed through numerical simulations that similar changes could be observed in a more realistic spiking network model (**Figure 5C, right panel**). Since experimental findings are based on calcium signals, we compared the results from the spiking network to the average PMTH convolved with an asymmetric exponential kernel (**Figure 5C**, blue and orange curves for weak and strong inhibition respectively). We set the decay time of the kernel to 1s.

The consistency of our models with the experimental autocorrelograms further shows that the observed network dynamics and, in particular, the correlation undershoots are a result of recurrent perisomatic inhibition rather than a feedforward drive from upstream areas. In our model, the maturation of perisomatic inhibition alone is sufficient to induce a switch in network dynamics.

Maturation of perisomatic GABAergic innervation causes the transition from movement-driven to movement-inhibited CA1 activity

We last tested experimentally the hypothesis that the increase in perisomatic innervation is causally involved in the switch observed in CA1 dynamics. To do so, we looked for a way to impair or delay the development of PVBC axons into the *stratum pyramidale*. We reasoned that affecting the activity of SST-expressing CA1 neurons could affect the maturation of PVBCs given their role in coordinating early CA1 dynamics (Bocchio et al., 2020; Flossmann et al., 2019; Wester and McBain, 2016) and their contribution to the maturation of PV neurons (Su et al., 2020; Tuncdemir et al., 2016; Wang et al., 2019). To this aim, we chronically reduced activity in CA1 SST-expressing interneurons from P3 to P8 using an inhibitory chemogenetic approach (**Figure 6A**). To do so, intra-hippocampal viral injections of the inhibitory DREADD receptor (AAV9-hSyn-DIO-hM4D(Gi)-mCherry virus) were performed in one hippocampus of newborn *Sst-Cre* pups and chronic subcutaneous injections of either saline or CNO solution were administered from P3 to P8 (**Figure 6A**). In most cases, the inhibitory DREADD was expressed by SST-interneurons in the hippocampus and adjacent neocortex (in 12 out of the 16 pups included in this analysis). We tested whether chronic inhibition of neocortical SST-expressing interneurons was sufficient to affect the maturation of hippocampal PVBCs, by restricting DREADD receptor expression to neocortical SST-expressing interneurons and found no impact on Syt2 labelling in the hippocampus (n=2 mice, +15% and +3% of Syt2 labelling in the ipsilateral hemisphere relative to the contralateral). For this reason, we decided to combine the data from the 16 injected pups. We next quantified at P9 the relative

change in the surface of the pyramidal cell layer covered by Syt2 labelling in the ipsilateral side as compared to the contralateral side (**Figure 6B - third row**). We found a significant reduction in Syt2 labelling in the ipsilateral hippocampus of mice treated with CNO but not saline (**Figure 6B and 6C**, CNO, n=16, mean= -21%, one sample t-test, T=3.669, p=0.0023; Saline, n=6, mean =-8%, one sample t-test, T=0.897, p=0.41). We conclude that inhibiting SST-expressing interneurons significantly reduces perisomatic innervation from putative PVBCs in the CA1 *stratum pyramidale*.

We next probed the impact of such reduction on CA1 dynamics. To do so, we imaged five pups previously injected with CNO (from P3-8, **Figure 6C** green dots). Only pups with a strong reduction in Syt2 labelling were kept for further analysis (three out of five pups, **Figure 6C**, **Figure S5A**, mice 200128_210206_0, 210128_210206_1, and 210402_210411_1; mean effect: -42%, -45%, -39% respectively, p=0.0625, p=0.0625, p=0.0938 respectively) while others were analyzed separately (**Figure S5A**). Interestingly, movement in these three pups was followed by an increase in the percentage of active cells (**Figure 6D,** peak value: 3.1%). In addition, the proportion of inhibitor movements decreased (**Figure 6E**) in stark contrast with control conditions (**Figure 2A, B**, P9-10) as well as with the two pups in which Syt2 labelling was not significantly affected (**Figure S5A,** 210211_210220_0 and 210402_210411_2, mean effect: +15% and -18% respectively, p=0.31 and p=0.56 respectively**)**. In other words, we found a correlation between the amount of PVBC innervation in *stratum pyramidale* and CA1 dynamics at the beginning of the second postnatal week (**Figure S5B**). We conclude that the emergence of PVBCs innervation contributes to the switch in CA1 dynamics from movement-activated to movement-inhibited.

DISCUSSION:

Our results demonstrate that the end of the first postnatal week marks a salient step in the structural and functional development of mouse CA1, using a combination of *in vivo* calcium imaging, chemogenetics and viral tracing. Indeed, this first week inaugurates the emergence of internal CA1 dynamics with their disengagement from sensorimotor inputs through the rapid development and activation of somatic GABAergic inhibition. Given the importance of internal dynamics for hippocampal function and cortical circuits operation in general, this is likely to be a critical general step in the proper maturation of cognitive circuits.

Early postnatal calcium activity in CA1 is driven by sensorimotor inputs

We found that, until P7-9, spontaneous movements are followed by a significant peak in calcium events in the CA1 principal cell layer and that most neuronal activity occurs during synchronous calcium events.

This early link between sensorimotor inputs and early cortical dynamics has been previously reported using electrophysiological recordings in various areas and species, including humans. Here we extend that observation to calcium transients, which, not only indirectly report action-potential firing as well as other modes of cell activation during development but also critically regulate activity-dependent genetic processes. In addition, we could describe the response to these movements with single-cell resolution. It is possible that other movements, like whisker movements, that we have not detected also contribute to the patterning of CA1 activity. It is also possible that self-generated activity from other sensory organs but independent from movement, like the retina or the olfactory bulb, also contribute to hippocampal dynamics, the same way they are relayed to sensory cortices. Interestingly, in contrast to previous reports (Tiriac et al., 2014), we did not observe any difference between twitches, occurring mainly during active sleep or longer movements. This may reveal a difference between calcium imaging and electrophysiology, the former sampling from a larger population but at a lower temporal and spike signal resolution. The patterning of CA1 dynamics in the large population imaged did not reveal any obvious spatial distribution for movement-activated cells but we cannot exclude that these would vary along the radial and transverse directions, which are the two main axes of principal cell development (Caviness, 1973), and are differentially targeted by perisomatic PV basket cells (Lee et al., 2014; Valero et al., 2015).

After P7-9, we observed a significant decrease in the fraction of coactive principal cells following movement (while interneurons remained mostly activated by movement). We cannot exclude that some spikes were falling below the threshold for detection of calcium events. In this case, rather than full inhibition, it may be that we observe a strong shortening of the time window for neuronal integration due to feedback inhibition that would limit the number of spikes produced by principal cells and keep them below calcium detection. Yet, we have used a novel machine-learning based algorithm (Denis et al., 2020) especially designed to early hippocampal dynamics in the dense pyramidal cell layer.

This “internalization” of hippocampal dynamics is reminiscent of similar phenomena observed in other cortical areas, such as the barrel cortex where whisker stimulation induces a reduction in the size of cell assemblies following P9 while the same stimulation widens cell assembly size a few days before (Mòdol et al., 2019). It also goes in hand with a sparsification of activity, which is a general developmental process supported by the emergence of inhibition (Golshani et al., 2009; Rochefort et al., 2009; Wolfe et al., 2010).

Circuit basis for the switch

Our results demonstrate that the internalization of CA1 dynamics occurring at the end of the first postnatal week most likely relies on structural changes in local CA1 circuits rather than rewiring of the long-range extrahippocampal connectivity.

The long-range circuits mediating the bottom-up flow of self-triggered or externally generated sensory information to cortical circuits and the hippocampus in particular are starting to be elucidated. The two main structures directly transmitting sensorimotor information to the dorsal CA1 are the entorhinal cortex and septum. The former processes multisensory information from all sensory cortices (visual, auditory, olfactory, somatosensory), including movement-related sensory feedback (Rio-Bermudez and Blumberg, 2021) and was shown to be activated by spontaneous twitches prior to CA1 (Mohns and Blumberg, 2010; Rio-Bermudez et al., 2020; Valeeva et al., 2019) while the latter is more likely to be involved in transmitting internal information (Fuhrmann et al., 2015; Wang et al., 2015) as well as unexpected environmental stimuli (Zhang et al., 2018). In addition to these two canonical pathways, one cannot exclude the involvement of a direct connection from the brainstem, given their existence in the adult and their role in promoting sleep as well as motor twitches (Liu et al., 2017; Szőnyi et al., 2019). However, our retrograde tracing experiments did not reveal any direct connection between the CA1 cells and the brainstem at the early ages analyzed here. In addition, we found that both CA1 interneurons and principal cells received inputs from the septum and entorhinal cortex before the time of the switch (i.e. P9) and that there was no major qualitative change of inputs after, as expected from previous work (Supèr and Soriano, 1994). Still, these experiments do not allow a quantitative assessment of the number of inputs nor the type of inputs (GABAergic, cholinergic, etc.) and we cannot fully exclude that a stronger, or different source of excitatory drive would be impinging onto interneurons after the switch. Therefore, future optogenetic and slice physiology work is needed to characterize the bottom-up information flow onto specific components of the local CA1 circuits. Similarly, one cannot exclude a change in the CA3 to CA1 connectivity. Indeed, Schaffer collaterals are known to reach CA1 roughly around the end of the first postnatal week (Durand et al., 1996). In addition, roughly at the time of the switch, do we see the emergence of SWRs (Buhl and Buzsaki, 2005), a pattern strongly relying on CA3 inputs and perisomatic GABAergic transmission. However, we could not restrict the pool of starter cells to the CA1 region in our retrograde viral tracing experiments, which precluded analysis of the development of CA3-CA1 connectivity.

As indicated by our model and our chemogenetic experiments, the disengagement from movement of CA1 dynamics can be fully explained by the observed rise in anatomical (Syt2 labelling)

and functional (axonal GCaMP imaging) connectivity from perisomatic GABAergic cells onto pyramidal cells at the onset of the second postnatal week. This increased connectivity could not be easily captured with our retrograde viral labelling since the absence of early PV expression precludes the identification of PV basket cells among retrogradely labelled cells in *Emx1Cre* pups. Early anatomical studies had already indicated that an increase of somatic GABAergic inhibition in CA1 occurred during the first postnatal week (Danglot et al., 2006; Jiang et al., 2001; Marty et al., 2002; Morozov and Freund, 2003). However, this rise was expected to be more progressive and not as abrupt as observed here, as it happened within two days.

Interestingly, a similar rise of somatic GABAergic axonal coverage occurs in the barrel cortex at the same time. Indeed, recent connectomic mapping using 3D-electron microscopy in that region revealed that the preferential targeting of cell bodies by GABAergic synapses increased almost threefold between postnatal days 7 and 9 (Gour et al., 2020), whereas two-photon imaging of putative GABAergic somatic axons in the same region revealed broader domains of co-activation (Mòdol et al., 2019). This time period for the shift may be synchronous within brain regions involved in sensorimotor integration such as the hippocampus and somatosensory cortex. Otherwise, PV innervation was shown to develop sequentially in a region-specific manner (Reh et al., 2020) following their intrinsic developmental age (Donato et al., 2017)

We found that many principal cells are inhibited by movement during the second postnatal week. The net effect of GABAergic perisomatic transmission observed here after the first postnatal week is therefore inhibitory. This is expected since the shift from excitatory to inhibitory synaptic transmission was reported to occur earlier in the hippocampus *in vivo* (Murata and Colonnese, 2020). The early excitatory GABAergic drive in CA1 circuits is therefore likely to originate from non-somatic GABAergic interneurons, which include long-range, dendrite-targeting or interneuron-specific interneurons. The circuit role of excitatory GABAergic transmission should be revisited taking into account this new finding.

Such movement-associated inhibition can result equally from feedforward (direct activation from movement-transmitting inputs such as the entorhinal cortex) or feedback (from local CA1 cells) inhibition. Our experiments do not allow disentangling both circuits. The progressive strengthening of feedback inhibition from local CA1 principal cells onto perisomatic GABAergic neurons is quite likely, as it occurs in the developing somatosensory cortex (Anastasiades and Butt, 2012). The inhibition of activity following movement is likely to be occurring during a transient developmental period. Indeed, in the adult, both interneurons and principal cells usually increase their activity as the animal moves

(Fuhrmann et al., 2015). Therefore the switch observed here opens another developmental time-window, that probably closes with the emergence of perineuronal nets and cell activation sequences at the end of the third developmental week (Farooq and Dragoi, 2019; Horii-Hayashi et al., 2015; Muessig et al., 2019). We would like to propose this developmental window, to be the critical period for CA1 development, a period during which experience-dependent plasticity can be observed.

Role of SST cells in the development of somatic inhibition

This study reveals an intriguing link between the activity of hippocampal SST-expressing neurons and the maturation of perisomatic GABAergic axonal coverage. Indeed, the chemogenetic inhibition of SST cells resulted in a significant decrease in Syt2 labelling, an indirect marker of prospective PV-expressing basket cells (Sommeijer and Levelt, 2012). We cannot exclude that the anatomical maturation of other interneurons, including soma-targeting CCK-expressing basket cells which develop anatomically at around the same time (Morozov and Freund, 2003), would also be affected by this manipulation. In fact, our computational model indicates that the emergence of feed-back inhibition is sufficient to reproduce the developmental shift observed here.

The critical developmental role of SST-neurons calcium activity is in agreement with the fact that the development of perisomatic GABAergic axons is an activity-dependent process (Chattopadhyaya et al., 2007; Huang, 2009). It is also reminiscent of how ablation or loss of function of deep-layer SST cells prevents the development of feedforward thalamic inputs onto PV cells in the layer 5 of somato-sensory cortex (Tuncdemir et al., 2016). Similarly, ablation of early born interneurons, which comprise a subpopulation of SST cells, prevents the development of functional GABAergic transmission during the first postnatal week in the developing mouse somatosensory cortex (Wang et al., 2019). The nature of the communication between SST and PV cells in the developing CA1 remains an open question. In the developing barrel cortex, SST neurons were shown to provide transient strong synaptic inputs onto PV neurons (Tuncdemir et al., 2016). In the adult, SST and PV cells are reciprocally connected with SST cells contacting PV neurons but in turn, some SST neurons, including O-LM cells do not receive PV inputs (Lovett-Barron et al., 2012). They may also transiently communicate through electrical synapses (Crépel et al., 2007), due to their common ontogenic origin (Yu et al., 2012).

One appealing hypothesis could be that SST cells, which comprise hub neurons (Bocchio et al., 2020; Bonifazi et al., 2009; Picardo et al., 2011) and promote synchronous activity in the developing CA1 (Bocchio et al., 2020; Flossmann et al., 2019) would relay sensorimotor inputs to local circuits and impact PV activity and anatomical development through their coordination of local CA1 dynamics. Of note, the CA1 SST cell population is extremely diverse and if comprised of O-LM, bistratified, and long-range

GABAergic interneurons (Pelkey et al., 2017). Therefore, whether specific subtypes of SST neurons are critically involved in this process remains an open question. The type of SST activity, and their specific contribution to early CA1 dynamics *in vivo* also remain unknown. Still, the action of SST-neurons may not necessarily imply modulation of neuronal activity. It could involve a direct trophic action of GABA, SST or other factors. Indeed, GABA released from SST neurons was shown to contribute to synaptogenesis (Oh et al., 2016). This could involve a paracrine mechanism by which SST-cells orchestrate the development of perisomatic inhibitory synapse through the production of collagen XIX, as recently established in the neocortex (Su et al., 2020).

One last interesting possibility could be that SST synapses would redirect future PV synapses to the soma of principal cells. This would fit with the decline of dendritic GABAergic coverage observed at around the same time point (Jiang et al., 2001) as well as with the recent finding that cell body GABAergic innervation could be established by the removal of inadequately placed synapses (Gour et al., 2020).

Conclusion

Cognitive hippocampal maps rely on two forms of representation, one that is map-based or allocentric and the other that is self-referenced, or egocentric and requires body movement. We would like to propose that the early postnatal period described here, where the hippocampus learns the statistics of the body, and which terminates with the rise of a recurrent inhibitory network is a key step for the emergence of an internal model onto which exploration of the external world can be grafted. An imbalance between internal and environmental hippocampal representations due to a miswiring of local somatic inhibition could have major outcomes. It could be at the basis of several neurodevelopmental disorders, including autism spectrum disorders (ASD) and schizophrenia. Interestingly, both disorders have been associated with an aberrant maturation of PV-expressing interneurons (Gogolla et al., 2014; Jurgensen and Castillo, 2015; Lewis et al., 2005). In addition, the proper development of the peripheral sensory system, which is partly initiating the early CA1 dynamics reported in our study, is also critically involved in ASD (Orefice et al., 2016). The period described here corresponds to the third trimester of gestation and likely extends postnatally given the protracted integration of GABAergic interneurons into functional circuits in the human brain (Murphy et al., 2005; Paredes et al., 2016). Future work should determine when a similar rise in somatic inhibition occurs in human infants and test whether it could constitute a valuable biomarker for cognitive neurodevelopmental disorders.

ACKNOWLEDGMENTS:

This work was supported by the European Research Council under the European Union's, Horizon 2020 research and innovation program Grant#646925, the Fondation Bettencourt Schueller, and a NWB seed grant # R20046AA. The project leading to this publication has received funding from the « Investissements d'Avenir » French Government program managed by the French National Research Agency (ANR-16-CONV-0001) and from Excellence Initiative of Aix-Marseille University - A*MIDEX. R.F.D. and E.L. are funded by the "Ministere de l'Enseignement Supérieur, de la Recherche et de l'Innovation". E.L. is funded by A*Midex foundation and the French National Research Agency funded by the French Government « Investissements d'Avenir » program (NeuroSchool, nEURo*AMU, ANR-17-EURE-0029 grant). J.D. was supported by the Fondation pour la Recherche Médicale Grant FDM20170638339. M.P was supported by the Fondation pour la Recherche Médicale Grant ARF20160936186. T. D and T. S. were funded by « Investissements d'Avenir » French Government program managed by the French National Research Agency (ANR-16-CONV-0001) and from Excellence Initiative of Aix-Marseille University - A*MIDEX. We would like to thank Dr. Pierre-Pascal Lenck-Santini for providing valuable feedback on our research project. We also would like to thank Marion Sicre for her help with *GAD67Cre* experiments. We are grateful to Pr. Hannah Monyer and Dr. Elodie Fino for providing the *GAD67Cre* and *SstCre* mouse lines respectively. We thank the Centre de Calcul Intensif d'Aix-Marseille for granting access to its high-performance computing resources. The rabies virus was a gift from Conzelman laboratory.

AUTHORS CONTRIBUTION:

RFD, MAP, and R.C designed research. RFD and EL performed viral injections, RFD and MAP performed two photon calcium imaging experiments. CL, MK, AB, RFD and MAP performed histology experiments. MM, RFD and MAP performed electrophysiological recordings, MM analyzed these recordings. RFD, JD, MAP, and R.C designed the analysis pipeline, RFD and JD, wrote DeepCINAC, CICADA and RINGO algorithms. TS and TD wrote PyAmnesia. SRB and HR designed and simulated the network models. RFD, MAP and RC wrote the paper.

REFERENCE LIST:

Anastasiades, P.G., and Butt, S.J.B. (2012). A Role for Silent Synapses in the Development of the Pathway from Layer 2/3 to 5 Pyramidal Cells in the Neocortex. Journal of Neuroscience *32*, 13085–13099.

Ben-Ari, Y. (2002). Excitatory actions of gaba during development: the nature of the nurture. Nature Reviews Neuroscience *3*, 728–739.

Bezaire, M.J., and Soltesz, I. (2013). Quantitative assessment of CA1 local circuits: Knowledge base for interneuron-pyramidal cell connectivity. Hippocampus *23*, 751–785.

Bocchio, M., Gouny, C., Angulo-Garcia, D., Toulat, T., Tressard, T., Quiroli, E., Baude, A., and Cossart, R. (2020). Hippocampal hub neurons maintain distinct connectivity throughout their lifetime. Nature Communications *11*, 1–19.

Bonifazi, P., Goldin, M., Picardo, M.A., Jorquera, I., Cattani, A., Bianconi, G., Represa, A., Ben-Ari, Y., and Cossart, R. (2009). GABAergic Hub Neurons Orchestrate Synchrony in Developing Hippocampal Networks. Science *326*, 1419–1424.

Broussard, G.J., Liang, Y., Fridman, M., Unger, E.K., Meng, G., Xiao, X., Ji, N., Petreanu, L., and Tian, L. (2018). In vivo measurement of afferent activity with axon-specific calcium imaging. Nat Neurosci *21*, 1272–1280.

Buhl, D.L., and Buzsaki, G. (2005). Developmental emergence of hippocampal fast-field "ripple" oscillations in the behaving rat pups. Neuroscience *134*, 1423–1430.

Buzsáki, G. (2015). Hippocampal sharp wave-ripple: A cognitive biomarker for episodic memory and planning. Hippocampus *25*, 1073–1188.

Buzsáki, G., and Moser, E.I. (2013). Memory, navigation and theta rhythm in the hippocampal-entorhinal system. Nature Neuroscience *16*, 130–138.

Caviness, V.S. (1973). Time of neuron origin in the hippocampus and dentate gyrus of normal and reeler mutant mice: an autoradiographic analysis. The Journal of Comparative Neurology *151*, 113–120.

Chattopadhyaya, B., Cristo, G.D., Wu, C.Z., Knott, G., Kuhlman, S., Fu, Y., Palmiter, R.D., and Huang, Z.J. (2007). GAD67-Mediated GABA Synthesis and Signaling Regulate Inhibitory Synaptic Innervation in the Visual Cortex. Neuron *54*, 889–903.

Crépel, V., Aronov, D., Jorquera, I., Represa, A., Ben-Ari, Y., and Cossart, R. (2007). A Parturition-Associated Nonsynaptic Coherent Activity Pattern in the Developing Hippocampus. Neuron *54*, 105–120.

Danglot, L., Triller, A., and Marty, S. (2006). The development of hippocampal interneurons in rodents. Hippocampus *16*, 1032–1060.

Denis, J., Dard, R.F., Quiroli, E., Cossart, R., and Picardo, M.A. (2020). DeepCINAC: A Deep-Learning-Based Python Toolbox for Inferring Calcium Imaging Neuronal Activity Based on Movie Visualization. Eneuro *7*, ENEURO.0038-20.2020.

Doischer, D., Hosp, J.A., Yanagawa, Y., Obata, K., Jonas, P., Vida, I., and Bartos, M. (2008). Postnatal Differentiation of Basket Cells from Slow to Fast Signaling Devices. Journal of Neuroscience *28*, 12956–12968.

Donato, F., Jacobsen, R.I., Moser, M.-B., and Moser, E.I. (2017). Stellate cells drive maturation of the entorhinal-hippocampal circuit. Science eaai8178-17.

Dooley, J.C., Glanz, R.M., Sokoloff, G., and Blumberg, M.S. (2020). Self-Generated Whisker Movements Drive State-Dependent Sensory Input to Developing Barrel Cortex. Curr Biol *30*, 2404-2410.e4.

Durand, G.M., Kovalchuk, Y., and Konnerth, A. (1996). Long-term potentiation and functional synapse induction in developing hippocampus. Nature *381*, 71–75.

Farooq, U., and Dragoi, G. (2019). Emergence of preconfigured and plastic time-compressed sequences in early postnatal development. Science *363*, 168–173.

Flossmann, T., Kaas, T., Rahmati, V., Kiebel, S.J., Witte, O.W., Holthoff, K., and Kirmse, K. (2019). Somatostatin Interneurons Promote Neuronal Synchrony in the Neonatal Hippocampus. CellReports *26*, 3173-3182.e5.

Fuhrmann, F., Justus, D., Sosulina, L., Kaneko, H., Beutel, T., Friedrichs, D., Schoch, S., Schwarz, M.K., Fuhrmann, M., and Remy, S. (2015). Locomotion, Theta Oscillations, and the Speed-Correlated Firing of Hippocampal Neurons Are Controlled by a Medial Septal Glutamatergic Circuit. Neuron *86*, 1253–1264.

Gogolla, N., Takesian, A.E., Feng, G., Fagiolini, M., and Hensch, T.K. (2014). Sensory Integration in Mouse Insular Cortex Reflects GABA Circuit Maturation. Neuron *83*, 894–905.

Golshani, P., Goncalves, J.T., Khoshkhoo, S., Mostany, R., Smirnakis, S., and Portera-Cailliau, C. (2009). Internally Mediated Developmental Desynchronization of Neocortical Network Activity. Journal of Neuroscience *29*, 10890–10899.

Gour, A., Boergens, K.M., Heike, N., Hua, Y., Laserstein, P., Song, K., and Helmstaedter, M. (2020). Postnatal connectomic development of inhibition in mouse barrel cortex. Science eabb4534-21.

Graf, J., Zhang, C., Marguet, S.L., Herrmann, T., Flossmann, T., Hinsch, R., Rahmati, V., Guenther, M., Frahm, C., Urbach, A., et al. (2021). A limited role of NKCC1 in telencephalic glutamatergic neurons for developing hippocampal network dynamics and behavior. Proc National Acad Sci *118*, e2014784118.

Gramsbergen, A., Schwartze, P., and Prechtl, H.F.R. (1970). The postnatal development of behavioral states in the rat. Dev Psychobiol *3*, 267–280.

Hopfield, J.J. (1982). Neural networks and physical systems with emergent collective computational abilities. Proc National Acad Sci *79*, 2554–2558.

Hopfield, J., and Tank, D. (2005). Computing with neural circuits: a model. Science *233*, 625–633.

Horii-Hayashi, N., Sasagawa, T., Matsunaga, W., and Nishi, M. (2015). Development and Structural Variety of the Chondroitin Sulfate Proteoglycans-Contained Extracellular Matrix in the Mouse Brain. Neural Plast *2015*, 1–12.

Huang, Z.J. (2009). Activity-dependent development of inhibitory synapses and innervation pattern: role of GABA signalling and beyond. The Journal of Physiology *587*, 1881–1888.

Inácio, A.R., Nasretdinov, A., Lebedeva, J., and Khazipov, R. (2016). Sensory feedback synchronizes motor and sensory neuronal networks in the neonatal rat spinal cord. Nature Communications *7*, 13060.

Jiang, M., Oliva, A.A., Lam, T., and Swann, J.W. (2001). GABAergic neurons that pioneer hippocampal area CA1 of the mouse: morphologic features and multiple fates. The Journal of Comparative Neurology *439*, 176–192.

Jouvet-Mounier, D., and Astic, L. (1968). [Study of the course of sleep in the young rat during the 1st postnatal month]. Comptes Rendus Des Séances De La Société De Biologie Et De Ses Fil *162*, 119–123.

Jurgensen, S., and Castillo, P.E. (2015). Selective Dysregulation of Hippocampal Inhibition in the Mouse Lacking Autism Candidate Gene CNTNAP2. J Neurosci *35*, 14681–14687.

Karlsson, K.A.E., Mohns, E.J., Prisco, G.V. di, and Blumberg, M.S. (2006). On the co-occurrence of startles and hippocampal sharp waves in newborn rats. Hippocampus *16*, 959–965.

Khazipov, R., Khalilov, I., Tyzio, R., Morozova, E., Ben-Ari, Y., and Holmes, G.L. (2004). Developmental changes in GABAergic actions and seizure susceptibility in the rat hippocampus. European Journal of Neuroscience *19*, 590–600.

Kim, J.-Y., Grunke, S.D., Levites, Y., Golde, T.E., and Jankowsky, J.L. (2014). Intracerebroventricular Viral Injection of the Neonatal Mouse Brain for Persistent and Widespread Neuronal Transduction. J Vis Exp 51863.

Lee, S.-H., Marchionni, I., Bezaire, M., Varga, C., Danielson, N., Lovett-Barron, M., Losonczy, A., and Soltesz, I. (2014). Parvalbumin-Positive Basket Cells Differentiate among Hippocampal Pyramidal Cells. Neuron *82*, 1129–1144.

Lewis, D.A., Hashimoto, T., and Volk, D.W. (2005). Cortical inhibitory neurons and schizophrenia. Nature Reviews Neuroscience *6*, 312–324.

Liu, K., Kim, J., Kim, D.W., Zhang, Y.S., Bao, H., Denaxa, M., Lim, S.-A., Kim, E., Liu, C., Wickersham, I.R., et al. (2017). Lhx6-positive GABA-releasing neurons of the zona incerta promote sleep. Nature Publishing Group *548*, 1–24.

Lovett-Barron, M., Turi, G.F., Kaifosh, P., Lee, P.H., Bolze, F., Sun, X.-H., Nicoud, J.-F., Zemelman, B.V., Sternson, S.M., and Losonczy, A. (2012). Regulation of neuronal input transformations by tunable dendritic inhibition. Nature Neuroscience *15*, 423–430.

Marty, S., Wehrlé, R., Alvarez-Leefmans, F.J., Gasnier, B., and Sotelo, C. (2002). Postnatal maturation of Na+, K+, 2Cl- cotransporter expression and inhibitory synaptogenesis in the rat hippocampus: an immunocytochemical analysis. European Journal of Neuroscience *15*, 233–245.

Miri, A., Daie, K., Arrenberg, A.B., Baier, H., Aksay, E., and Tank, D.W. (2011). Spatial gradients and multidimensional dynamics in a neural integrator circuit. Nat Neurosci *14*, 1150–1159.

Mòdol, L., Bollmann, Y., Tressard, T., Baude, A., Che, A., Duan, Z.R.S., Babij, R., García, N.V.D.M., and Cossart, R. (2019). Assemblies of Perisomatic GABAergic Neurons in the Developing Barrel Cortex. Neuron 1–18.

Mohns, E.J., and Blumberg, M.S. (2008). Synchronous Bursts of Neuronal Activity in the Developing Hippocampus: Modulation by Active Sleep and Association with Emerging Gamma and Theta Rhythms. Journal of Neuroscience *28*, 10134–10144.

Mohns, E.J., and Blumberg, M.S. (2010). Neocortical Activation of the Hippocampus during Sleep in Infant Rats. Journal of Neuroscience *30*, 3438–3449.

Morozov, Y.M., and Freund, T.F. (2003). Postnatal development and migration of cholecystokinin-immunoreactive interneurons in rat hippocampus. Neuroscience *120*, 923–939.

Muessig, L., Lasek, M., Varsavsky, I., Cacucci, F., and Wills, T.J. (2019). Coordinated Emergence of Hippocampal Replay and Theta Sequences during Post-natal Development. Current Biology *29*, 834-840.e4.

Murata, Y., and Colonnese, M.T. (2020). GABAergic interneurons excite neonatal hippocampus in vivo. Science Advances *6*, eaba1430.

Murphy, K.M., Beston, B.R., Boley, P.M., and Jones, D.G. (2005). Development of human visual cortex: A balance between excitatory and inhibitory plasticity mechanisms. Dev Psychobiol *46*, 209–221.

Oh, W.C., Lutzu, S., Castillo, P.E., and Kwon, H.-B. (2016). De novo synaptogenesis induced by GABA in the developing mouse cortex. Science *353*, 1037–1040.

Orefice, L.L., Zimmerman, A.L., Chirila, A.M., Sleboda, S.J., Head, J.P., and Ginty, D.D. (2016). Peripheral Mechanosensory Neuron Dysfunction Underlies Tactile and Behavioral Deficits in Mouse Models of ASDs. Cell *166*, 299–313.

Pachitariu, M., Stringer, C., Dipoppa, M., Schröder, S., Rossi, L.F., Dalgleish, H., Carandini, M., and Harris, K.D. (2017). Suite2p: beyond 10,000 neurons with standard two-photon microscopy. Biorxiv 061507.

Paredes, M.F., James, D., Gil-Perotin, S., Kim, H., Cotter, J.A., Ng, C., Sandoval, K., Rowitch, D.H., Xu, D., McQuillen, P.S., et al. (2016). Extensive migration of young neurons into the infant human frontal lobe. Science *354*, aaf7073.

Paxinos, G., Halliday, G., Watson, C., and Kassem, M.S. (2020). Atlas of the Developing Mouse Brain (Academic Press).

Pelkey, K.A., Chittajallu, R., Craig, M.T., Tricoire, L., Wester, J.C., and McBain, C.J. (2017). Hippocampal GABAergic Inhibitory Interneurons. Physiological Reviews *97*, 1619–1747.

Picardo, M.A., Guigue, P., Allene, C., and Fishell, G. (2011). Pioneer GABA cells comprise a subpopulation of hub neurons in the developing hippocampus. Neuron *71*, 695–709.

Pnevmatikakis, E.A., and Giovannucci, A. (2017). NoRMCorre: An online algorithm for piecewise rigid motion correction of calcium imaging data. Journal of Neuroscience Methods *291*, 83–94.

Reh, R.K., Dias, B.G., Nelson, C.A., Kaufer, D., Werker, J.F., Kolb, B., Levine, J.D., and Hensch, T.K. (2020). Critical period regulation across multiple timescales. Proc National Acad Sci *117*, 23242–23251.

Rio-Bermudez, C.D., and Blumberg, M.S. (2021). Sleep as a window on the sensorimotor foundations of the developing hippocampus. Hippocampus.

Rio-Bermudez, C.D., Kim, J., Sokoloff, G., and Blumberg, M.S. (2020). Active Sleep Promotes Coherent Oscillatory Activity in the Cortico-Hippocampal System of Infant Rats. Cerebral Cortex (New York, N.Y. : 1991) *30*, 2070–2082.

Rochefort, N.L., Garaschuk, O., Milos, R.-I., Narushima, M., Marandi, N., Pichler, B., Kovalchuk, Y., and Konnerth, A. (2009). Sparsification of neuronal activity in the visual cortex at eye-opening. Proceedings of the National Academy of Sciences of the United States of America *106*, 15049–15054.

Soltesz, I., and Losonczy, A. (2018). CA1 pyramidal cell diversity enabling parallel information processing in the hippocampus. Nature Neuroscience *21*, 1–10.

Sommeijer, J.-P., and Levelt, C.N. (2012). Synaptotagmin-2 is a reliable marker for parvalbumin positive inhibitory boutons in the mouse visual cortex. PLoS ONE *7*, e35323.

Su, J., Basso, D., Iyer, S., Su, K., Wei, J., and Fox, M.A. (2020). Paracrine Role for Somatostatin Interneurons in the Assembly of Perisomatic Inhibitory Synapses. J Neurosci *40*, 7421–7435.

Suen, C.Y., Wang, P.S.P., LEE, S.-W., LAM, L., and SUEN, C.Y. (1994). Thinning Methodologies for Pattern Recognition. S Mach Perc 239–261.

Supèr, H., and Soriano, E. (1994). The organization of the embryonic and early postnatal murine hippocampus. II. Development of entorhinal, commissural, and septal connections studied with the lipophilic tracer DiI. The Journal of Comparative Neurology *344*, 101–120.

Szőnyi, A., Sos, K.E., Nyilas, R., Schlingloff, D., Domonkos, A., Takács, V.T., Pósfai, B., Hegedüs, P., Priestley, J.B., Gundlach, A.L., et al. (2019). Brainstem nucleus incertus controls contextual memory formation. Science *364*, eaaw0445-15.

Tiriac, A., Del Rio-Bermudez, C., and Blumberg, M.S. (2014). Self-Generated Movements with "Unexpected" Sensory Consequences. Curr Biol *24*, 2136–2141.

Tuncdemir, S.N., Wamsley, B., Stam, F.J., Osakada, F., Goulding, M., Callaway, E.M., Rudy, B., and Fishell, G. (2016). Early Somatostatin Interneuron Connectivity Mediates the Maturation of Deep Layer Cortical Circuits. Neuron *89*, 521–535.

Tyzio, R., Represa, A., Jorquera, I., Ben-Ari, Y., Gozlan, H., and Aniksztejn, L. (1999). The Establishment of GABAergic and Glutamatergic Synapses on CA1 Pyramidal Neurons is Sequential and Correlates with the Development of the Apical Dendrite. 1–11.

Valeeva, G., Janackova, S., Nasretdinov, A., Rychkova, V., Makarov, R., Holmes, G.L., Khazipov, R., and Lenck-Santini, P.-P. (2019). Emergence of Coordinated Activity in the Developing Entorhinal-Hippocampal Network. Cerebral Cortex (New York, N.Y. : 1991) *29*, 906–920.

Valero, M., Cid, E., Averkin, R.G., Aguilar, J., Sanchez-Aguilera, A., Viney, T.J., Gomez-Dominguez, D., Bellistri, E., and Prida, L.M. de la (2015). Determinants of different deep and superficial CA1 pyramidal cell dynamics during sharp-wave ripples. Nature Neuroscience *18*, 1281–1290.

Villette, V., Malvache, A., Tressard, T., Dupuy, N., and Cossart, R. (2015). Internally Recurring Hippocampal Sequences as a Population Template of Spatiotemporal Information. Neuron *88*, 357–366.

Vormstein-Schneider, D., Lin, J.D., Pelkey, K.A., Chittajallu, R., Guo, B., Arias-Garcia, M.A., Allaway, K., Sakopoulos, S., Schneider, G., Stevenson, O., et al. (2020). Viral manipulation of functionally distinct interneurons in mice, non-human primates and humans. Nature Neuroscience *23*, 1–21.

Wang, C.-Z., Ma, J., Xu, Y.-Q., Jiang, S.-N., Chen, T.-Q., Yuan, Z.-L., Mao, X.-Y., Zhang, S.-Q., Liu, L.-Y., Fu, Y., et al. (2019). Early-generated interneurons regulate neuronal circuit formation during early postnatal development. ELife *8*, 333.

Wang, Y., Romani, S., Lustig, B., Leonardo, A., and Pastalkova, E. (2015). Theta sequences are essential for internally generated hippocampal firing fields. Nature Neuroscience *18*, 282–288.

Wester, J.C., and McBain, C.J. (2016). Interneurons Differentially Contribute to Spontaneous Network Activity in the Developing Hippocampus Dependent on Their Embryonic Lineage. The Journal of Neuroscience : The Official Journal of the Society for Neuroscience *36*, 2646–2662.

Wickersham, I.R., Lyon, D.C., Barnard, R.J.O., Mori, T., Finke, S., Conzelmann, K.-K., Young, J.A.T., and Callaway, E.M. (2007). Monosynaptic Restriction of Transsynaptic Tracing from Single, Genetically Targeted Neurons. Neuron *53*, 639–647.

Wolfe, J., Houweling, A.R., and Brecht, M. (2010). Sparse and powerful cortical spikes. Current Opinion in Neurobiology *20*, 306–312.

Yu, Y.-C., He, S., Chen, S., Fu, Y., Brown, K.N., Yao, X.-H., Ma, J., Gao, K.P., Sosinsky, G.E., Huang, K., et al. (2012). Preferential electrical coupling regulates neocortical lineage-dependent microcircuit assembly. Nature 1–6.

Yuste, R. (2015). From the neuron doctrine to neural networks. Nat Rev Neurosci *16*, 487–497.

Zhang, G.-W., Sun, W.-J., Zingg, B., Shen, L., He, J., Xiong, Y., Tao, H.W., and Zhang, L.I. (2018). A Non-canonical Reticular-Limbic Central Auditory Pathway via Medial Septum Contributes to Fear Conditioning. Neuron *97*, 406-417.e4.

Figure 1

A

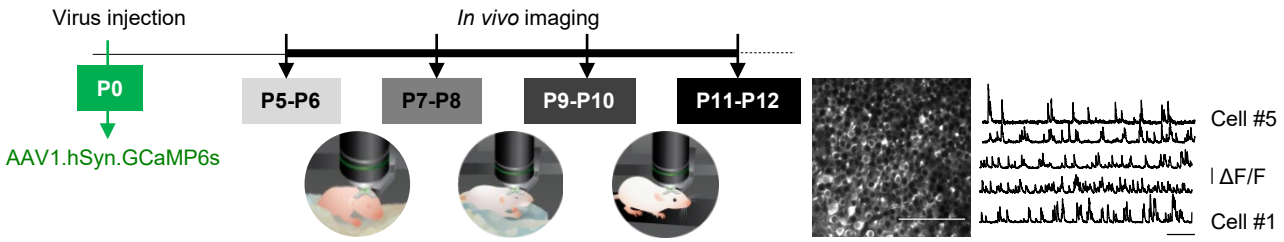

B

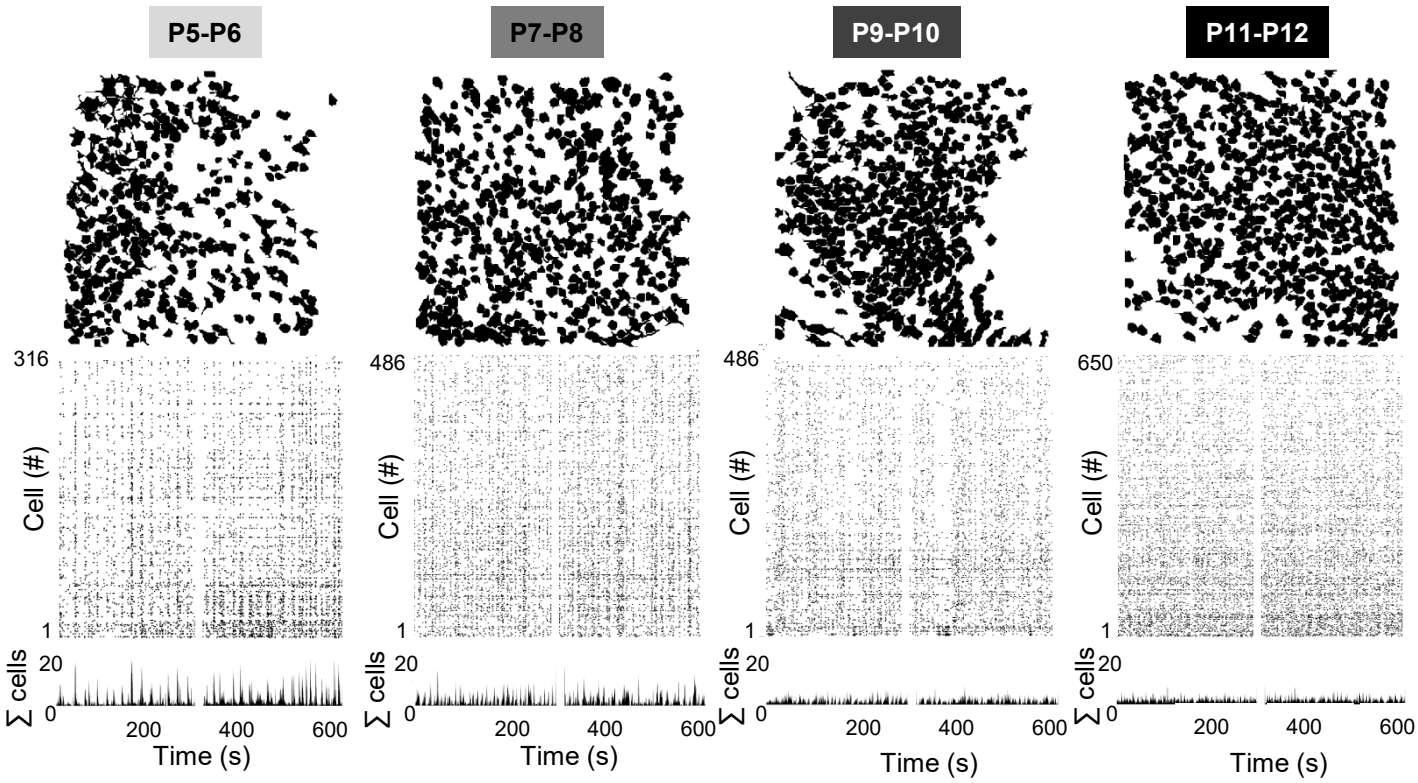

C

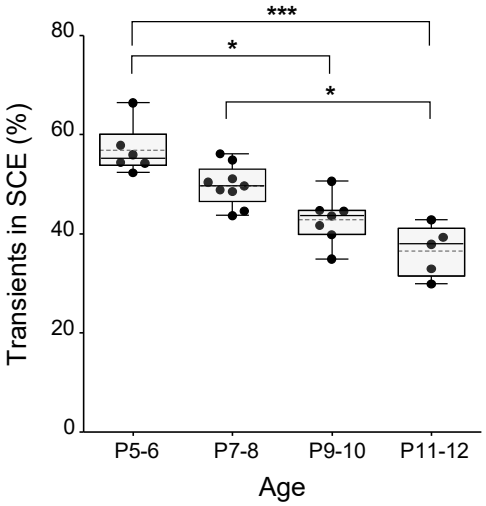

D

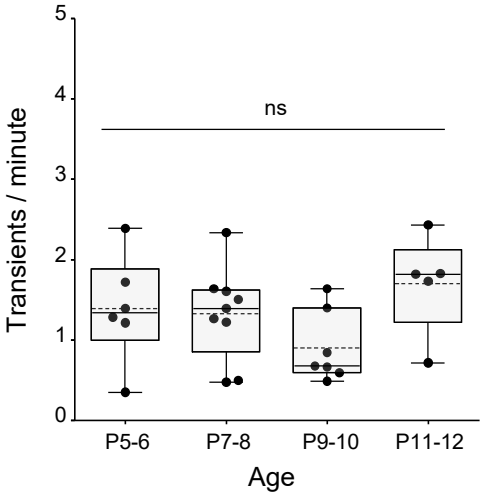

Figure 1: Imaging CA1 dynamics during the first two postnatal weeks.

(A). Schematic of the experimental timeline. On postnatal day 0 (P0), 2µL of viral solution are injected in the left lateral ventricle of mouse pups. From five to twelve days after injection (P5-P12), acute surgery for window implantation above the corpus callosum was performed followed by a session of 2-photon calcium imaging. The gap in the recordings occurring at approximately 250 s reflects 10 seconds long pauses for frame saving before consecutive acquisition blocks.

(B). Top row: Example contour maps of imaged neurons from fields of view of P5, P7, P10 and P12 mouse pups. Middle row: raster plots showing neuronal activity as a function of time. Bottom row: Graph representing the sum of active cells as a function of time.

(C). Distribution of the ratio of neuronal transients within SCEs over the total number of transients. Each dot represents the mean cell event during SCE divided by the total cell event ratio from all cells imaged in one mouse. Each boxplot shows the 25th, 50th and 75th percentiles and whiskers represent the 5th to the 95th percentile. The dashed gray line represents the mean of the distribution. A significant age effect was detected (Kruskal-Wallis test, KW stat = 19.51, p-value = 0.0002). Significant difference between P5-6 (n=6) and P9-10 (n=7), between P5-6 (n=6) and P11-12 (n=5), as well as between P7-8 (n=9) and P11-12 (n=5) were observed (Dunn's multiple comparisons test, * p-value < 0.05, *** p-value < 0.001).

(D). Distribution of the number of transients per minute across the two first postnatal weeks. Each dot represents the mean transient frequency from all cells imaged in one animal. Each boxplot shows the 25th, 50th and 75th percentiles and whiskers represent between the 5th to the 95th percentile. The dashed gray line represents the mean of the distribution. No significant influence of the age was found (Kruskal-Wallis test, KW stat = 6.166, p-value = 0.1038).

Figure 2

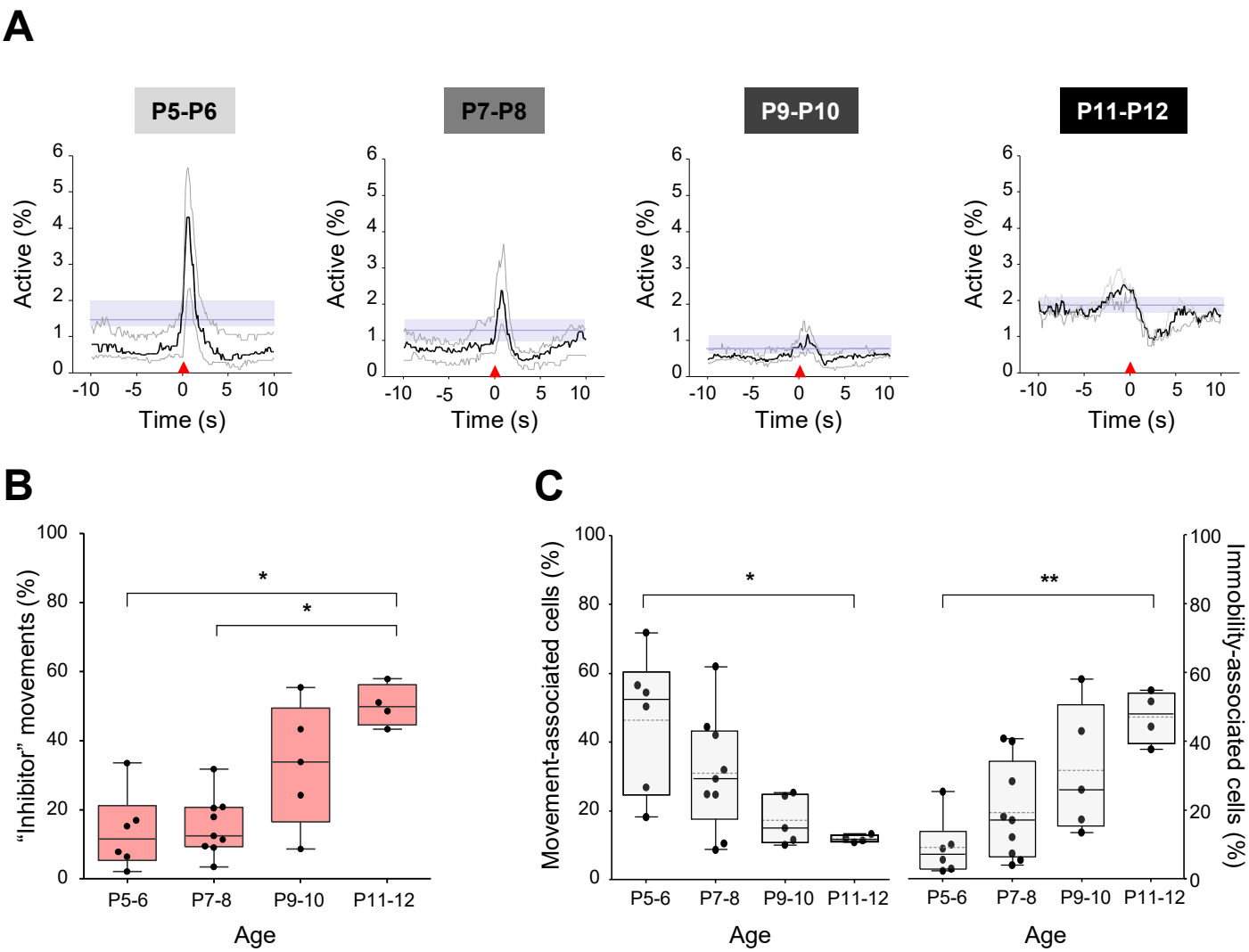
A
P5-P6
P7-P8
P9-P10
P11-P12
Active (%)
Time (s)
B
"Inhibitor" movements (%)
Age
P5-6
P7-8
P9-10
P11-12
C
Movement-associated cells (%)
Immobility-associated cells (%)
*
**

Figure 2: Linking CA1 dynamics to movement during the first two postnatal weeks.

(A). Peri-Movement-Time-Histograms (PMTH) centered on the onset of the mouse movements (red triangle). For each age group, all movement onsets were aligned to time 0 and the number of active cells was averaged across all pups within a 20 seconds-long time window centered on the onset of movement. The dark line indicates the median value, the two grey lines represent the 25th and 75th percentiles (P5-6: N=6, n=11, 4829 cells, 1406 movements, P7-8: N=9, n=17, 10477 cells, 2557 movements, P9-10: N=5, n=10, 6271 cells, 902 movements, P11-12: N=4, n=5, 2816 cells, 313 movements. N: number of mice, n: number of fields of view). In all panels the light blue area delineates the 25th and 75th percentiles of the proportion of active cells resulting from surrogate raster plots; the dark blue line shows the median obtained from the surrogates.

(B). Distribution of the proportion of movements followed by a decrease of activity ('inhibitor' movements). Each boxplot shows the 25th, 50th and 75th percentiles with whiskers from the 5th to the 95th percentile. Each dot represents a mouse. (P5-P6: n=6, P7-P8: n=9, P9-P10: n=5, P11-P12: n=4). A significant effect of age was detected (age effect Kruskall-Wallis test, KS-stat: 12.10, p=0.0071) with the proportion of "inhibitor" movements being higher in P11-12 than both P5-6 and P7-8 mice (Dunn's test 5-6 vs 11-12 and 7-8 vs 11-12 $p < 0.05$).

(C). Distribution of the proportion of movement- (left panel) and immobility- associated cells (right panel) as a function of age. Each dot represents a mouse. Each boxplot shows the 25th, 50th and 75th percentiles with whiskers from the 5th to the 95th percentile. The dashed gray line represents the mean of the distribution. The proportion of movement-associated cells is significantly correlated to the age (Kruskal-Wallis test, KS-stat= 9.825, p-value=0.0201). Post-hoc Dunn's multiple comparison test shows a significant difference between P5-6 and P11-12 (p-value < 0.05). The proportion of immobility-associated cells is significantly correlated with age (Kruskal-Wallis test, KS-stat=12.03, p-value=0.0073). Post-hoc Dunn's multiple comparison test shows a significant difference between P5-6 and P11-12 (p-value < 0.01).

Figure 3

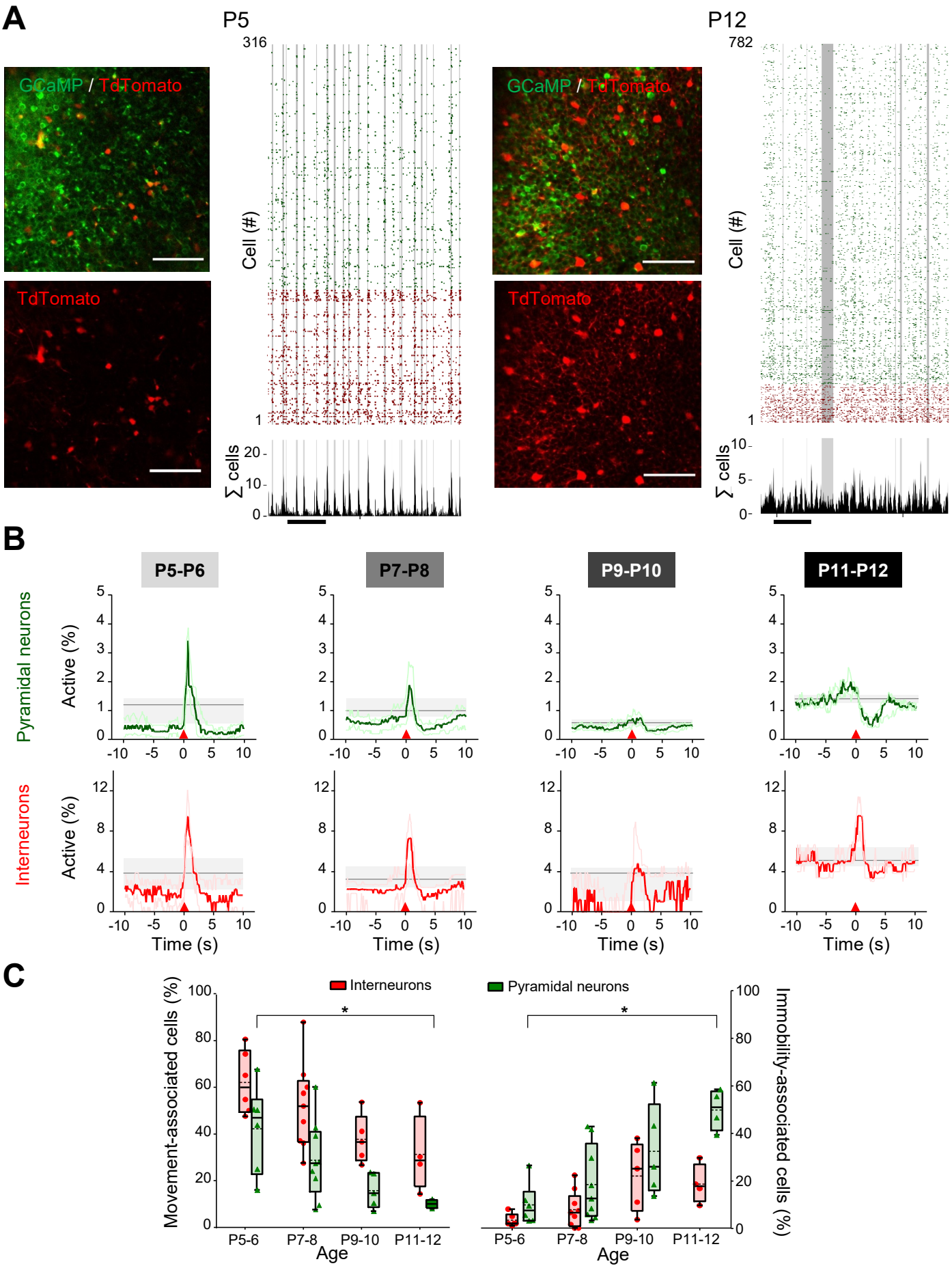
A
P5
P12
GCaMP / TdTomato
TdTomato
316
782
Cell (#)
1
∑ cells
20
10
0
5
B
P5-P6
P7-P8
P9-P10
P11-P12
Pyramidal neurons
Interneurons
Active (%)
Time (s)
C
Interneurons
Pyramidal neurons
Movement-associated cells (%)
Immobility-associated cells (%)
Age
P5-6
P7-8
P9-10
P11-12
*

Figure 3: Differential recruitment of CA1 glutamatergic and GABAergic neurons

(A). Imaged field of view and associated raster plot from example imaging sessions in the *stratum pyramidale* from P5 (left) and P12 (right) mouse pups (scale bars= 100µm). Imaged neurons expressed GCaMP6s. Interneurons were identified by the expression of the red reporter tdTomato. In the raster plots neurons are sorted according to their identification as pyramidal cells (green) or interneurons (red). Below graph represents the fraction of active cells as a function of time. Scale bar: 60 seconds.

(B). Peri-Movement-Time-Histograms centered on the onset of the mouse movements (red triangle). For each age group, all movement onsets were aligned to time 0 and the number of active pyramidal cells (green - top row) or active interneurons (red - bottom row) was averaged across all pups within a 20 seconds-long time window centered on the onset of movement. The dark green and red lines indicate the median value, and the two light green and red lines represent the 25th and 75th percentiles (P5-6: N=6, n=11, 4179 pyramidal cells, 650 GABAergic cells, 1406 movements, P7-8: N=9, n=17, 9551 pyramidal cells, 926 GABAergic cells, 2557 movements, P9-10: N=5, n=10, 5965 pyramidal cells, 306 GABAergic cells, 902 movements, P11-12: N=4, n=5, 2527 pyramidal cells, 289 GABAergic cells, 313 movements. N: number of mice, n: number of imaging field of view). In all panels the light grey area delineates the 25th and 75th percentiles of the proportion of active cells resulting from surrogate raster plots, dark grey line shows the median obtained from the surrogates.

(C). Boxplots showing the proportion of movement- (left panel) and immobility-associated cells (right panel). Pyramidal cells are displayed in green, interneurons in red. A significant age effect was detected in the association between pyramidal cells and both movement and immobility (movement: Kruskall-Wallis test, KS-stat=10.68, p=0.0136; immobility: Kruskall-Wallis test, KS-stat=11.66, p=0.0086). Post-hoc multiple comparison tests show a significant difference between P5-6 and P11-12 for both movement and immobility associated-pyramidal cells (Dunn's test, p-value < 0.05).

Figure 4

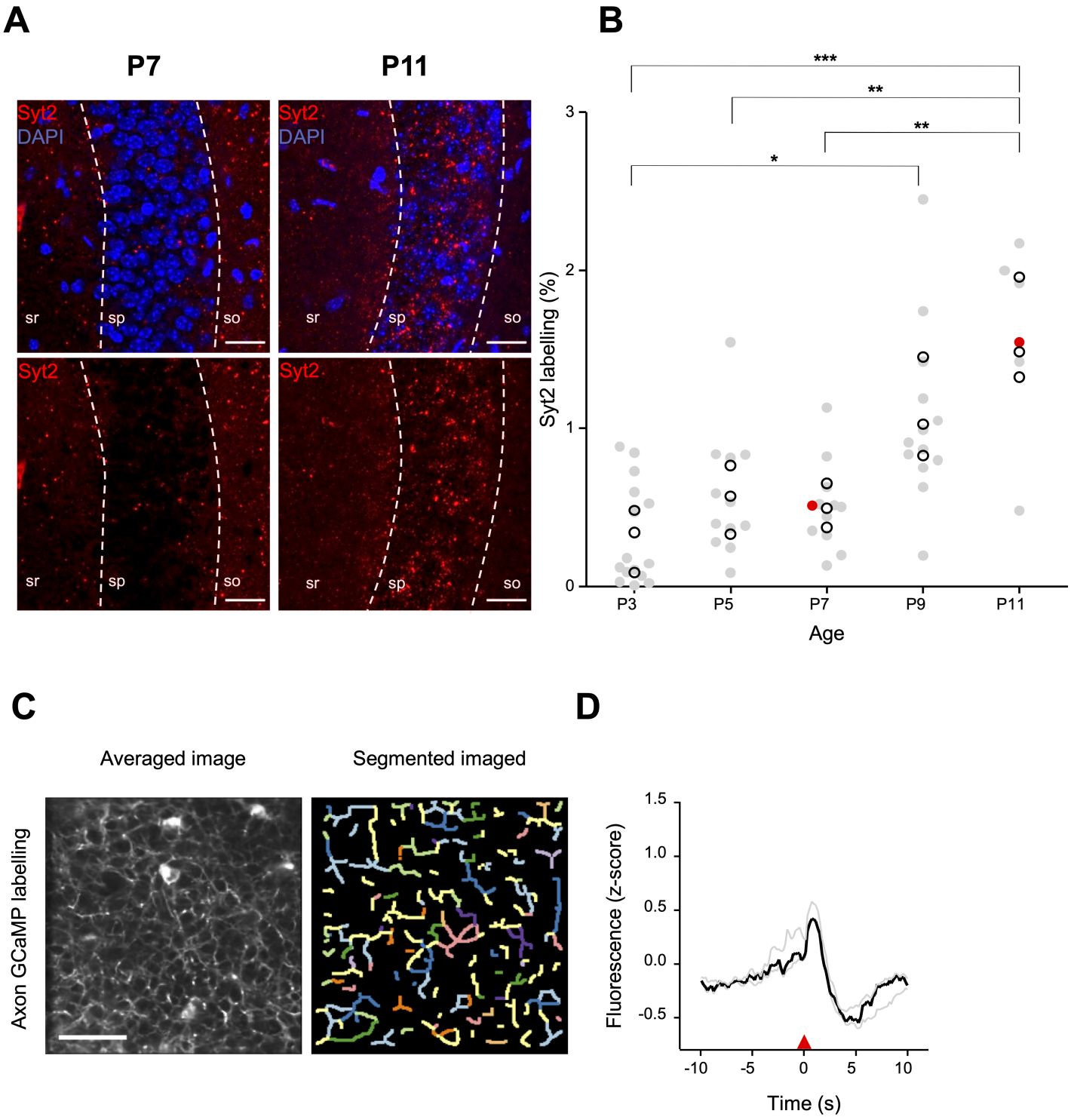
A
P7
P11
Syt2
DAPI
sr
sp
so
B
***
**
**
*
Syt2 labelling (%)
0
1
2
3
P3
P5
P7
P9
P11
Age
C
Averaged image
Segmented imaged
Axon GCaMP labelling
D
Fluorescence (z-score)
1.5
1.0
0.5
0.0
-0.5
-10
-5
0
5
10
Time (s)

Figure 4: Emergence of perisomatic GABAergic innervation

(A). Representative example confocal images of the CA1 region in a P7 (left) and a P11 (right) mouse pup. DAPI staining was used to delineate the *stratum pyramidale* (sp) from the *stratum radiatum* (sr) and *stratum oriens* (so, top row). Synaptotagmin-2 labelling (Syt2) is shown in the top and bottom rows. Illustrated examples are indicated by red dots in the associated quantification in (B). Scale bar= 20 µm.

(B). Fraction of the pyramidal cell layer covered by Syt2 positive labelling as a function of age. Each gray dot represents the average percentage of coverage from two images taken in the CA1 region of a hippocampal slice. Open black dots are the average values across brain slices from one mouse pup. Red dots indicate the slices used for illustration in (A). A significant effect of age was detected (One-Way Anova, $F=13.11$, $p=0.0005$). Multiple comparison test shows a significant difference between age groups (Bonferroni's test, *: $p<0.05$, **: $p<0.01$, ***: $p<0.001$).

(C). Averaged image of a field of view in the pyramidal cell layer of a P9 *GAD67Cre* mouse pup injected with a Cre-dependent Axon-GCaMP6s indicator (left) and the segmented image resulting from PyAmnesia (right).

(D). Peri-movement time histogram showing the average fluorescence signal centered on the onsets of animal movement (red triangle; N=3, n=3, 506 movements, 104 axonal branches). The dark grey line indicates the median value, and the light grey lines represent 25th and 75th percentile.

Figure 5

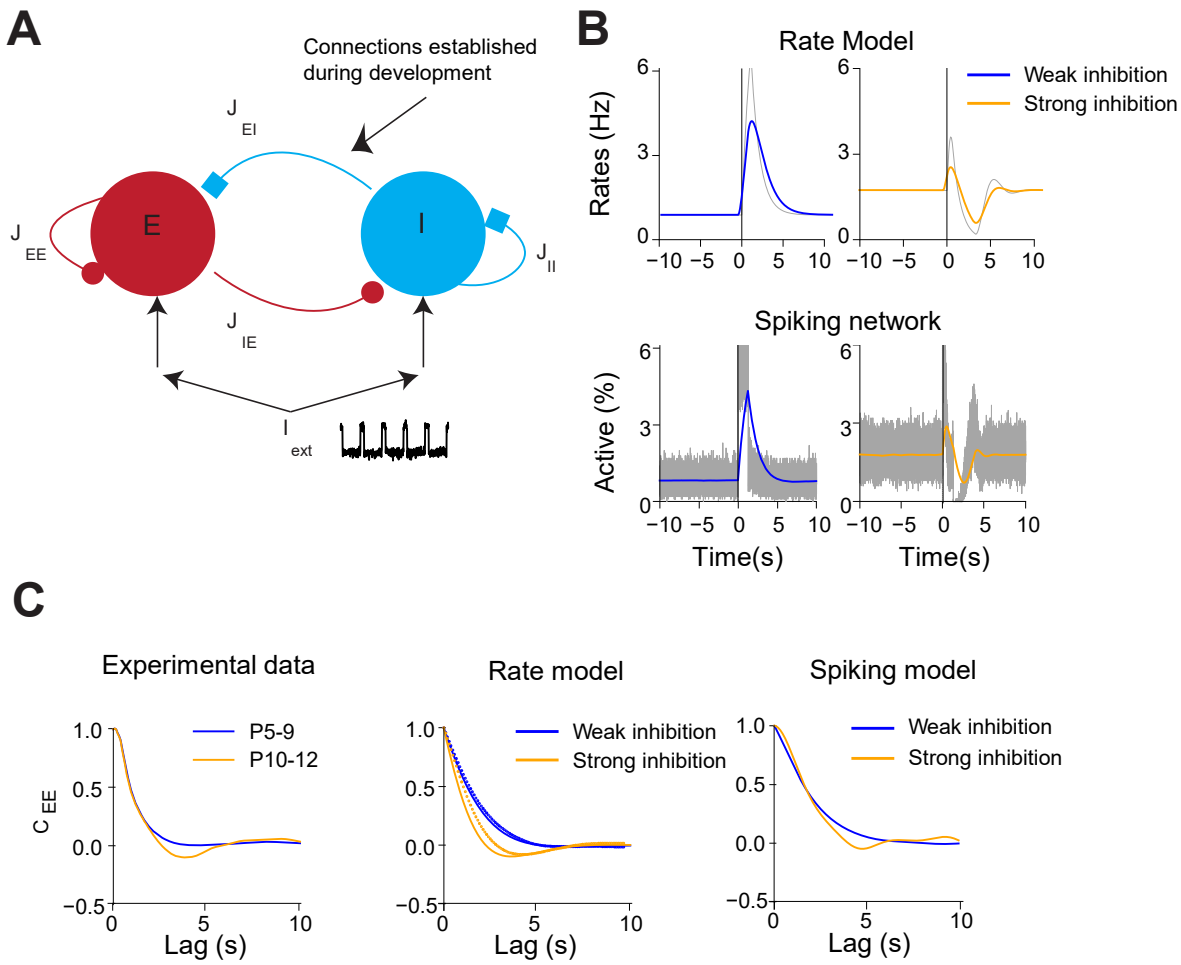
A
Connections established during development
J EI
J EE
J IE
J II
E
I
I ext
B
Rate Model
Rates (Hz)
Weak inhibition
Strong inhibition
Spiking network
Active (%)
Time(s)
Time(s)
C
Experimental data
Rate model
Spiking model
C EE
P5-9
P10-12
Weak inhibition
Strong inhibition
Weak inhibition
Strong inhibition
Lag (s)
Lag (s)
Lag (s)

Figure 5: Modelling the effects of perisomatic inhibition on pyramidal cell response

(A). The model consists of two populations, Excitatory (E) and Inhibitory (I) receiving feedforward input I_{ext}. The interaction strengths, Jab represent the effect of the activity of population b on a. We study the effects of perisomatic inhibition on the activity of pyramidal cells by varying the parameter JEI.

(B). PMTH, response of excitatory neurons to pulse input in the rate model (top row) and LIF network (bottom row). Individual responses are in gray. Solid lines are PMTH convolved with an exponential kernel of 1s (approximate Gcamp6s timescale). Weak inhibition on the left (blue) and strong inhibition on the right (orange).

(C). Correlations in data (left), rate model (middle), and LIF network (right). In the rate model, solid lines are the predicted correlation from the analytic expressions and open circles are the results from numerical integration.

Figure 6

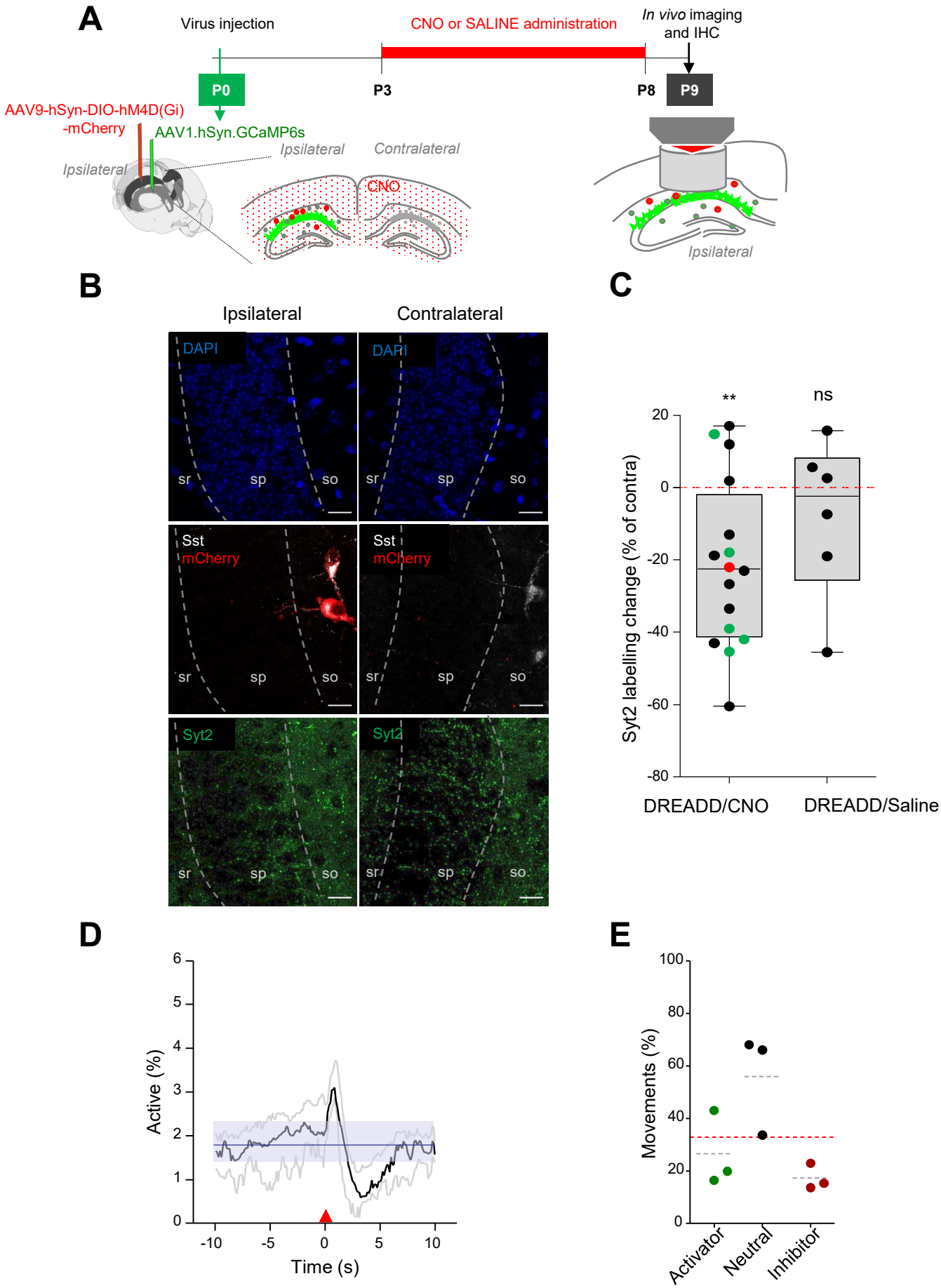
A
Virus injection
CNO or SALINE administration
In vivo imaging and IHC
P0
P3
P8
P9
AAV9-hSyn-DIO-hM4D(Gi) -mCherry
AAV1.hSyn.GCaMP6s
Ipsilateral
Contralateral
CNO
B
Ipsilateral
Contralateral
DAPI
sr
sp
so
Sst
mCherry
Syt2
C
**
ns
Syt2 labelling change (% of contra)
20
0
-20
-40
-60
-80
DREADD/CNO
DREADD/Saline
D
Active (%)
6
5
4
3
2
1
0
-10
-5
0
5
10
Time (s)
E
Movements (%)
100
80
60
40
20
0
Activator
Neutral
Inhibitor

Figure 6. Altering the development of perisomatic PV innervation prevents the transition from movement-activated to movement-inhibited activity.

(A). Experimental paradigm allowing for the chronic inhibition of SST-expressing interneurons. At P0 *Sst-Cre* mouse pups are co-injected with GCaMP6s (green) in the left lateral ventricle and with Cre-dependent hM4D(Gi) (red) in the left hippocampus. From P3 to P8 (included) mouse pups are subcutaneously injected every 8 hours with either CNO (10mg/kg) or saline. At P9, mouse pups are either sacrificed for immuno-histochemistry experiments or implanted with the hippocampal window for *in vivo* imaging prior to immuno-histochemistry experiments.

(B). Example confocal images from the CA1 region of the hippocampus of a P9 mouse pup injected with the inhibitory DREADD and treated with CNO for 5 days. Left panels show the ipsilateral (injected with DREADD) side, right panels show the contralateral side. DAPI labeling (top row) is used to delineate the *stratum pyramidale* (sp) from the *stratum radiatum* (sr) and *stratum oriens* (so). Middle row shows the colocalization of DREADD expression (red) and SST (white) on the ipsilateral side (left) and SST-expressing cells in the *stratum oriens* on the contralateral side (right). Bottom row shows Syt2 labeling (green) in the ipsilateral (left) and contralateral side (right). Scale bar: 20 µm

(C). Quantification of the Syt2 labeling on the ipsilateral side compared to the contralateral side in mouse pups after DREADD/CNO (left box plot) or DREADD/Saline (right box plot) treatment. Each dot represents a mouse pup. Green dots indicate the pups for which we performed 2-photon calcium imaging. Red point indicates the example depicted in figure 6B. Each boxplot shows the 25th, 50th and 75th percentiles with whiskers from the 5th to the 95th percentile. The mean was significantly lower than 0 in the CNO-treated group (One sample t-test, theoretical mean 0, T=3.84, p=0.0016)

(**D**). Peri-Movement-Time-Histograms centered on the onset of the animal movements (red triangle). Dark and grey lines display the evolution of the proportion of active cells in P9 mouse pups after chronic inhibition of SST-expressing cells. The light blue area delineates the 25th and 75th percentiles of the proportion of active cells resulting from surrogate raster plots; the dark blue line shows the median obtained from the surrogates.

(E). Distribution of the proportion of movements followed by an increase ('*activator*' movement, green), no change ('*neutral*' movement, gray) and by a decrease ('*inhibitor*' movement, red) of neuronal activity. Each dot represents a mouse pup. The dashed red line represents the mean proportion of "*inhibitor*" movements in P9-10 animals (figure 2B).

Figure S1

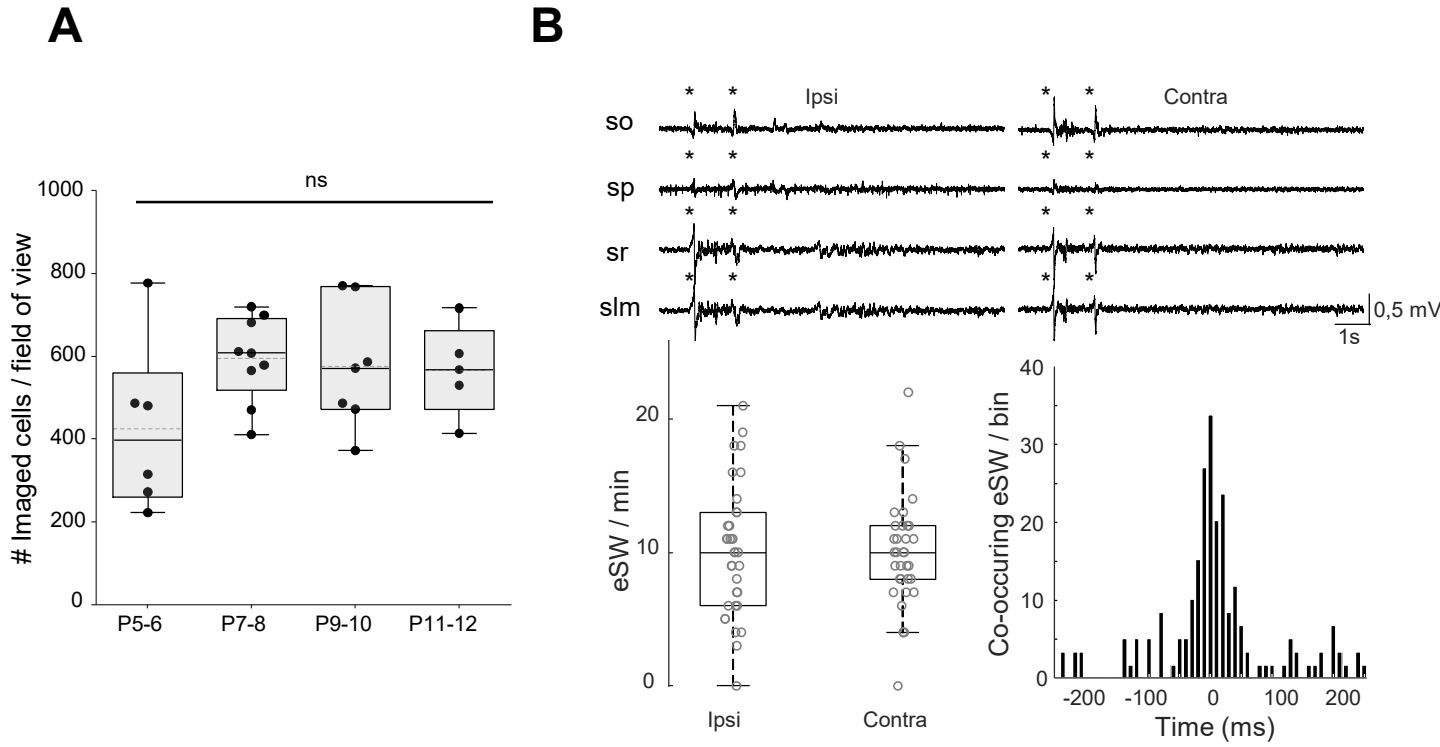
A
B
ns
Imaged cells / field of view
1000
800
600
400
200
0
P5-6
P7-8
P9-10
P11-12
Ipsi
Contra
so
sp
sr
slm
0,5 mV
1s
eSW / min
20
10
0
Ipsi
Contra
Co-occuring eSW / bin
40
30
20
10
0
-200
-100
0
100
200
Time (ms)

Figure S1: Experimental paradigm allows for stable and reliable calcium imaging.

(A). Distribution of the number of imaged cells across ages. Each dot represents a mouse. Each boxplot shows the 25th, 50th and 75th percentiles and whiskers represent the 5th to the 95th percentile. The dashed gray line represents the mean of the distribution.

(B). Top panels: Example of the electrophysiological recording done in the ipsi (hippocampus with window implant) and contralateral (intact hippocampus) hippocampi. Use of multisite silicon probe allowed simultaneous recordings in different hippocampal layers (*strati oriens* (so), *pyramidale* (sp), *radiatum* (sr) and *lacunosum moleculare* (slm)). The eSPW are marked by asterisks. Bottom left panel: Box plot displays the eSPW occurrence. Each dot represents the eSPW rate per minute in the 10 minutes period. Box plots show median (bold black line), the bottom and top edges of the box indicate the 25th and 75th percentiles, the whiskers extend to the most extreme data points not considered outliers. Bottom right panel: Co-occurrence of eSPW detected in both hippocampi.

Figure S2

A

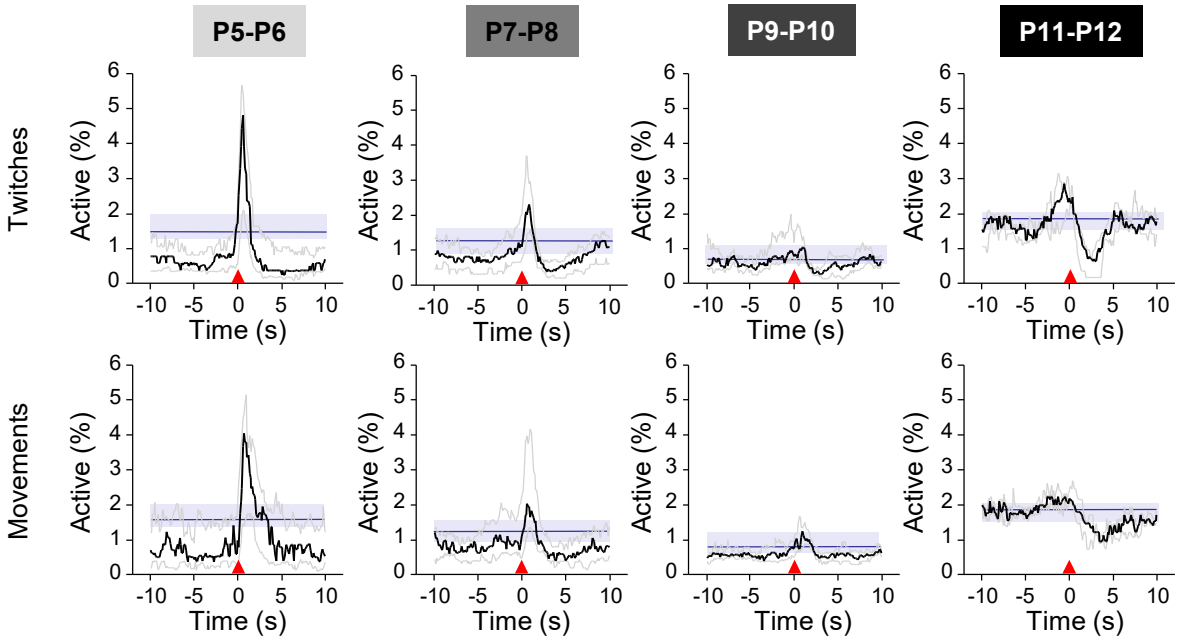
P5-P6
P7-P8
P9-P10
P11-P12
Twitches
Movements
Active (%)
Time (s)

B

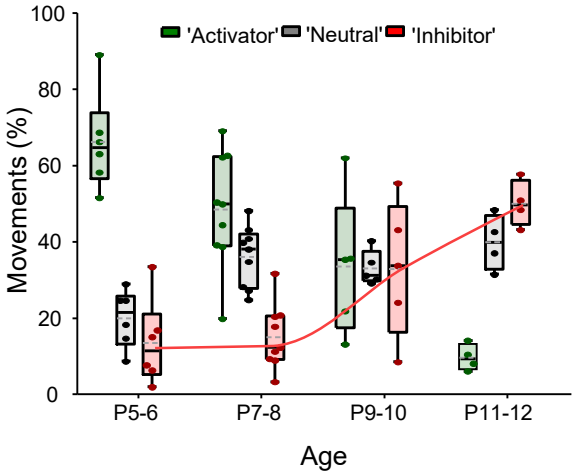
'Activator'
'Neutral'
'Inhibitor'
Movements (%)
P5-6
P7-8
P9-10
P11-12
Age

Figure S2: Linking CA1 dynamics to twitches and complex movements during the first two postnatal weeks.

(A). Peri-Movement-Time-Histograms (PMTH) centered on the onset of the animal movements (red triangles). For each age group, all onsets of movement are aligned to time 0 and the number of active cells is averaged across all mouse pups in a 20 second long window centered on the onset of mouse movement. The dark line indicates the median value, the two grey line represent 25th and 75th percentile (P5-6: N=6, n=11, 4829 cells, P7-8: N=9, n=17, 10477 cells, P9-10: N=5, n=10, 6271 cells, P11-12: N=4, n=5, 2816 cells. N: number of mice, n: number of imaging field of view). The top row shows PMTH obtained combining detected twitches, the bottom row shows PMTH obtained combining complex movement of the mice. In all panels the light blue area delineates the 25th and 75th percentiles of the proportion of active cells resulting from surrogate raster plots; the dark blue line shows the median obtained from the surrogates.

(B). Evolution of the proportion of "activator", "neutral" and "inhibitor" (respectively in green, grey and red) movements across development. Each dot represents a mouse. Each boxplot shows the 25th, 50th and 75th percentiles and whiskers represent the 5th to the 95th percentile. The red line represents the developmental increase of "inhibitor" movement.

Figure S3

A

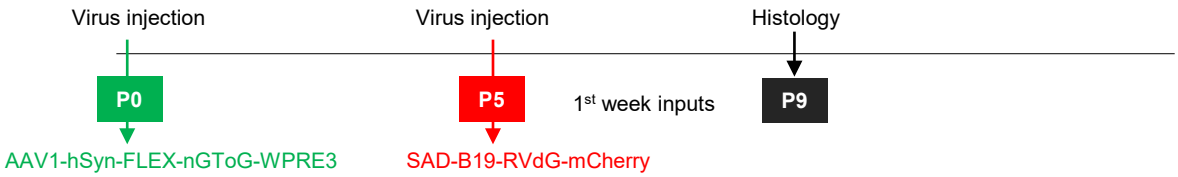

B

Gad67-Cre

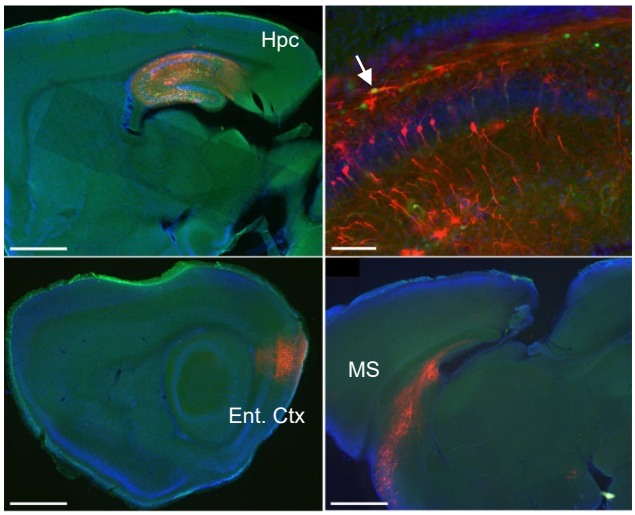

C

Emx1-Cre

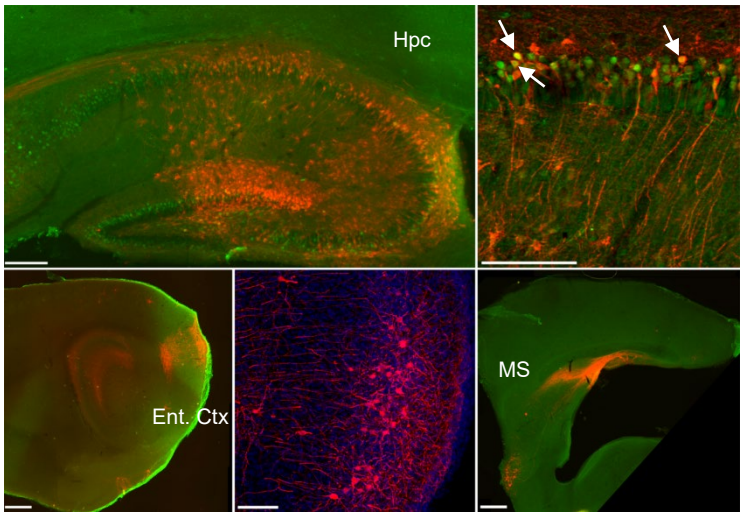

D

E

Gad67-Cre

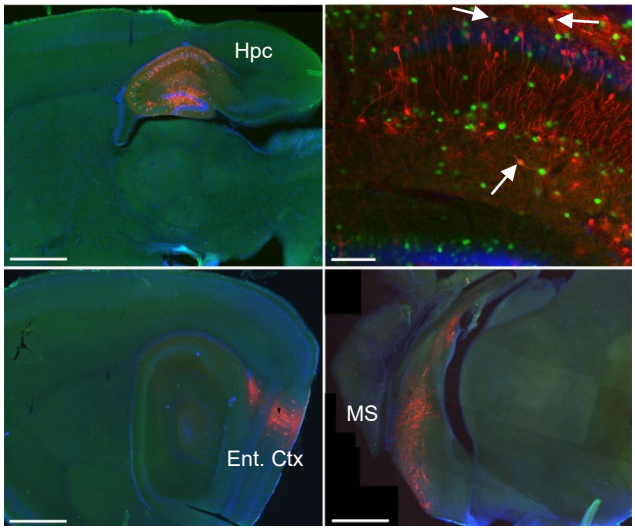

F

Emx1-Cre

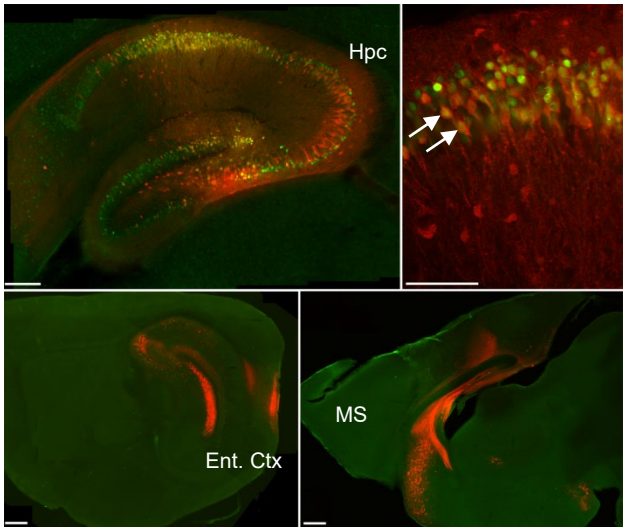

Figure S3: Monosynaptic retrograde tracing shows similar extra-hippocampal inputs onto both pyramidal cells and interneurons during the 2 first postnatal weeks.

(A). Experimental timeline used to investigate the inputs received by pyramidal cells (*Emx1Cre* mice) and interneurons (*GAD67Cre* mice) during the first postnatal week (early group). At P0 and P5 we injected the helper virus AAV1-hSyn-FLEX-nGToG-WPRE3 and the rabies SAD-B19-RVdG-mCherry into the hippocampus of *GAD67Cre* (Figure 3B) mice and *Emx1Cre* mice (Figure 3C) respectively. Brains are next collected for histological/anatomical analysis at P9.

(B). Confocal images from early group *GAD67Cre* mice showing the injection sites in the dorsal hippocampus at lower magnification (top left, scale bar= 1 mm), and higher magnification (top right, scale bar=100 µm). Primo infected cells are labelled in green, starter cell indicated by the arrow shows co-expression of the helper virus (green) and rabies virus (red). Presynaptic cells, labelled only in red, are localized in the entorhinal cortex (bottom left, scale bar= 1 mm) and in the medial septum (bottom right, scale bar= 1 mm). Hpc= Hippocampus; Ent. Ctx= Entorhinal Cortex; MS= Medial Septum

(C). same as in (B) but for *Emx1Cre* mice. Scale bars from top left to bottom right: 200 µm, 100 µm, 500µm, 100 µm and 500 µm. Middle bottom image is a higher magnification of bottom lef panel.

(D). Same as in (A) but for the late group (P9-P13).

(E). Same as in (B) but for the late group. Scale bars from top left to bottom right: 1 mm, 100 µm, 1 mm and 1mm.

(F). Same as in (C) but for the late group. Scale bars from top left to bottom right: 200 µm, 100 µm, 500µm, and 500 µm.

Figure S4

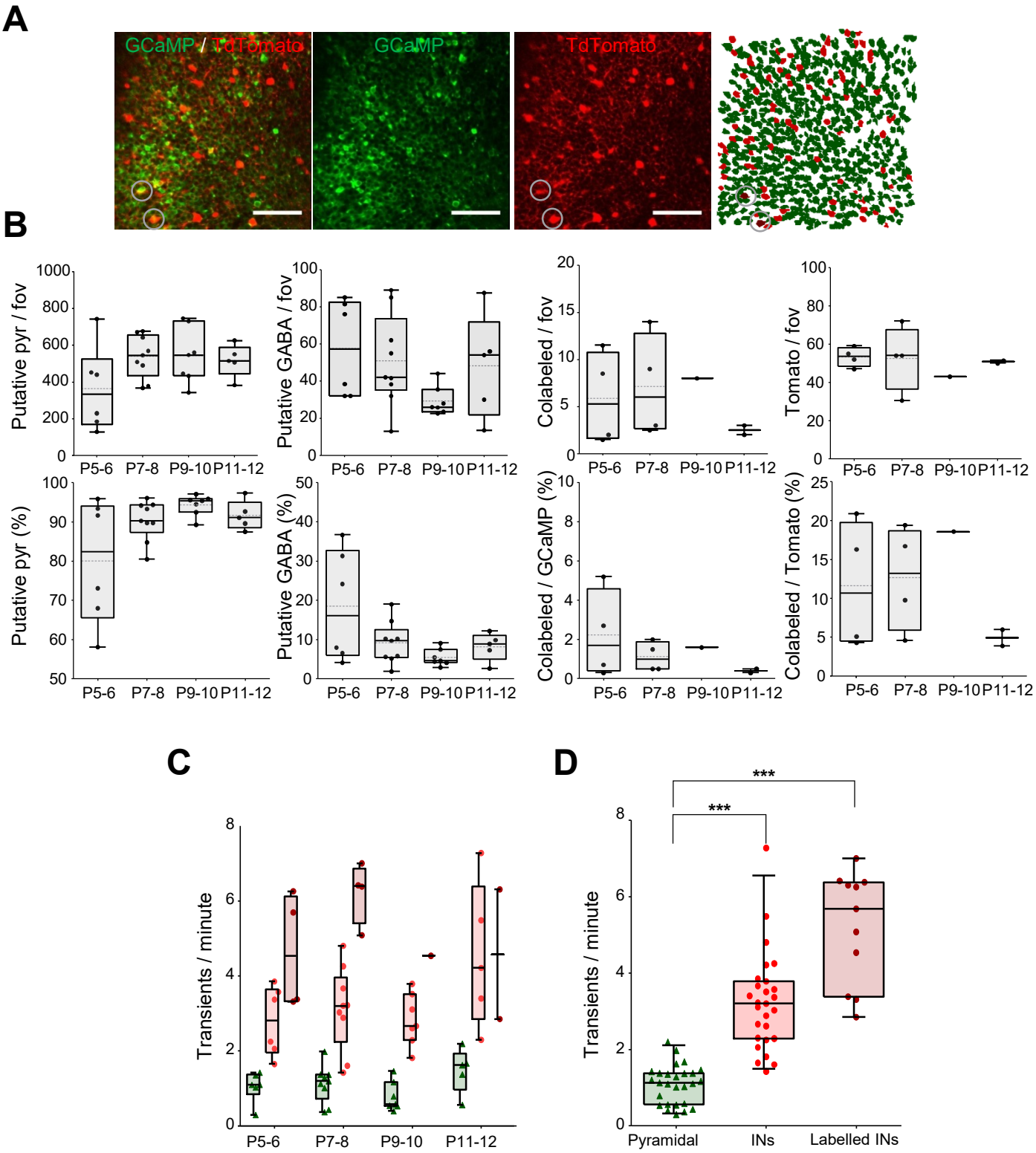
A
GCaMP / TdTomato
GCaMP
TdTomato
B
Putative pyr / fov
Putative GABA / fov
Colabeled / fov
Tomato / fov
Putative pyr (%)
Putative GABA (%)
Colabeled / GCaMP (%)
Colabeled / Tomato (%)
P5-6
P7-8
P9-10
P11-12
C
Transients / minute
D
***
***
Pyramidal
INs
Labelled INs

Figure S4. Combining labelled and inferred interneurons.

(A). Example field of view in a *GAD67Cre* mouse pups injected with both AAV.1-hSyn-GCAMP6s.WPRE.SV40 and AAV9-FLEX-CAG-tdTomato displaying co-infected cells (eg interneurons, circled in the first panel). Individual GCaMP6s and tdTomato signals are shown in the second and third panel. The last panel shows the contour map obtained on this field of view, pyramidal cells are represented in green, inferred interneurons are in red, labelled (tdTomato) interneurons are in dark red. Scale bars: 100 µm.

(B). Top row shows the mean number of putative pyramidal cells (first panel),inferred interneurons (second panel), co-infected cells (third panel) and tdTomato expressing cells (fourth panel) per field of view. The bottom row shows the proportion of putative pyramidal cells and inferred interneurons among all imaged cells (first and second panel) and the proportion of co-labelled cells among GCaMP expressing cells (third panel) or among tdTomato expressing cells (fourth panel). Each dot represents a mouse. Each boxplot shows the 25th, 50th and 75th percentiles and whiskers represent the 5th to the 95th percentile. The dashed grey lines represent the mean.

(C). Distribution of the number of transients per minute across the two first postnatal weeks. Each symbol represents the mean transient frequency from all putative pyramidal cells (green), inferred interneurons (red) and labelled interneurons (dark red) imaged in one animal. Each boxplot shows the 25th, 50th and 75th percentiles and whiskers represent the 5th to the 95th percentile.

(D). Distribution of the number of transients per minute in putative pyramidal cells (green), inferred interneurons (red) and labelled interneurons (dark red) irrespectively of the mouse age. Each symbol represents a mouse. Each boxplot shows the 25th, 50th and 75th percentiles and whiskers represent the 5th to the 95th percentile.

Figure S5

A

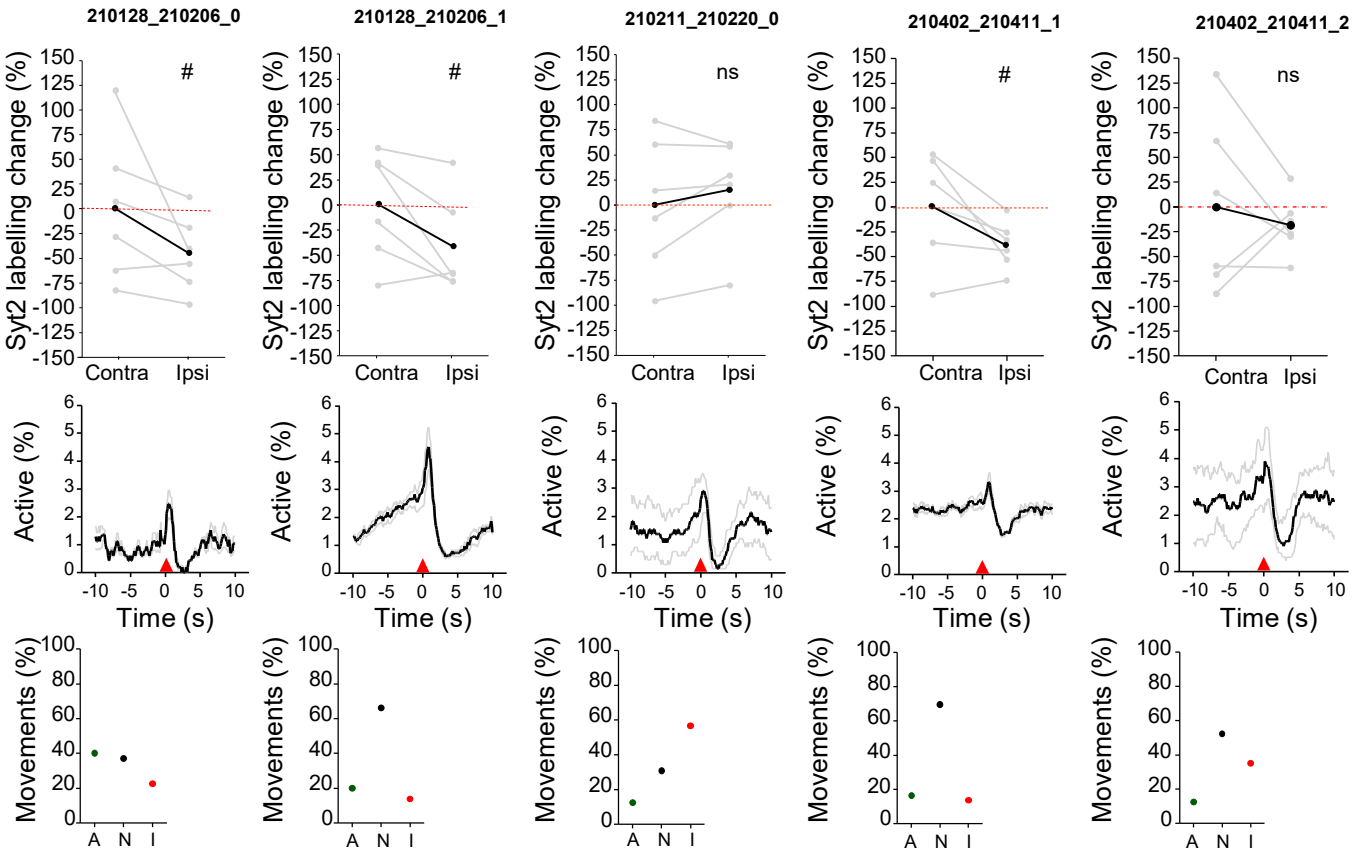
210128_210206_0
210128_210206_1
210211_210220_0
210402_210411_1
210402_210411_2
Syt2 labelling change (%)
#
ns
Contra
Ipsi
Active (%)
Time (s)
Movements (%)
A
N
I

B

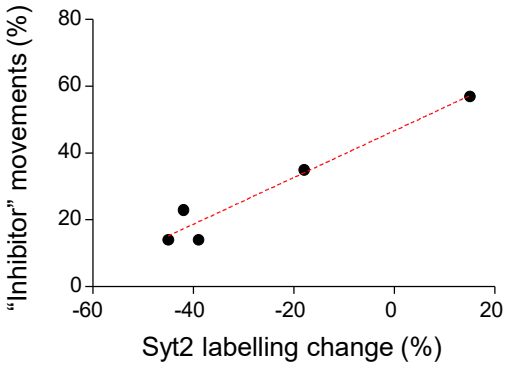
"Inhibitor" movements (%)
Syt2 labelling change (%)

Figure S5: Reduced development of perisomatic innervation correlates with reduced functional inhibition.

(A). Effect of chronic CNO injection on the five imaged mice (Five green dots displayed in Figure 6C). The top row shows the change in Syt2 labelling. Each grey dot represents the relative change of Syt2 labelling in a slice compare to the mean of the contralateral hemisphere. Grey line shows the appariement across slices. Black dots show the mean. For each mouse, Wilcoxon signed rank test was used to detect significant differences between ipsilateral and contralateral hemispheres. From left to right p-values (#) were respectively 0.0625, 0.0625, and 0.0938. Middle row shows the individual PMTH (peri-movement time histogram). Bottom row shows the proportion of "Activator" (A) movement, "Neutral" (N), "Inhibitor" (I) in each mouse.

(B). Scatter plot showing the percentage of "inhibitor" movement as a function of the change of Syt2 coverage in the ipsilateral hemisphere relative to the contralateral. Each dot represents a mouse. The dashed red line represent the linear correlation between the two variable (slope: 0.7003 ± 0.09176, p=0.0047, r-squared=0.9510)

Supplementary Movie 1: 2-photon calcium imaging movie from the example illustrated in Figure 1B, first panel (P5). Movie was sped up 10 times.

Supplementary Movie 2: 2-photon calcium imaging movie from the example illustrated in Figure 1B, second panel (P7). Movie was sped up 10 times.

Supplementary Movie 3: 2-photon calcium imaging movie from the example illustrated in Figure 1B, third panel (P10). Movie was sped up 10 times.

Supplementary Movie 4: 2-photon calcium imaging movie from the example illustrated in Figure 1B, last panel (P12). Movie was sped up 10 times.